Elastic helium scattering studies of ordered overlayers of Ar, Kr, and Xe physisorbed on Ag(111)

K. D. Gibson, C. Cerjan,[a] J. C. Light, and S. J. Sibener[b]

Department of Chemistry and The James Franck Institute, The University of Chicago, Chicago, Illinois 60637

We describe experiments that measured the angle resolved intensity of He ($E_i = 18$ and 66 meV) elastically scattering from the surfaces of rare gas overlayers physisorbed on Ag(111). These studies were done on a layer-by-layer basis for 1, 2, 3, and ~25 ordered overlayers of Ar, Kr, and Xe. Two types of experiments are described. The first is diffraction, where the scattered He intensity was measured as a function of the detector angle, with the incident polar and azimuthal angles held constant. In the second type of experiment, selective adsorption, we measured the specular intensity as a function of incident angle. The purpose of these experiments was to examine the He–surface potential, to assess the relative contributions that various He–rare gas pair potentials, nonadditive multibody terms, and He–substrate interactions make to the systems studied. The experiments are compared with the results of accurate close-coupling calculations, in order to quantitatively perform these assessments. The comparisons between the selective adsorption data and scattering calculations demonstrate the extreme sensitivity that such measurements have to the He–surface potential. In particular, observable changes in the calculated selective adsorption spectra appear when different He-rare gas potentials are tested, or when various nonadditive terms are included in the potential. The results suggest that further refinements in the He-heavy–rare gas pair potentials may be in order.

INTRODUCTION

This is the last in a series of papers in which we discuss our studies of ordered overlayers of rare gases physisorbed on Ag(111). To briefly reiterate, we used a supersonic beam of He atoms as our probe, and observed the angle resolved scattering from the surfaces of these structures. This was done on a layer-by-layer basis for 1, 2, 3, and ~25 or more ordered overlayers of physisorbed Ar, Kr, and Xe. These corrugated surfaces have many channels for elastic scattering, which occur at discrete final angles as determined by the Bragg relation. Inelastic scattering occurs outside of the first surface Brillouin zone due to this high corrugation. The low surface vibrational frequencies of these overlayers result in a large probability for inelastic scattering. Other than a short review article,[1] previous papers[2-6] have dealt only briefly with elastic scattering, being mainly concerned with single phonon inelastic scattering. In this paper, we will examine the elastic scattering experiments, and the information they contain, in detail. The data will also be compared with the results of accurate close-coupling calculations, using realistic He–surface potentials.

Interatomic forces are normally represented as an expansion over progressively higher order interactions, consisting of a sum over pair potentials plus a sum over three-body potential functions and so on. In the case of the inert gases, this expansion is often quickly truncated. Using only the sums of the pair potentials and the Axilrod–Teller–Muto triple–dipole interactions, the properties of solid Ar, Kr, and Xe can be reasonably explained, though this might be fortuitous.[7,8] In the case of the physisorbed rare gases, the interaction of the He with the Ag substrate must also be considered. Even for a monolayer, the distance of closest approach of the He atom to the substrate is fairly large, allowing the total two-body He–substrate interaction to be represented by an asymptotic van der Waals interaction. Multibody interactions which include the substrate can also be considered. Since the total potential is a periodic function of the surface atom coordinates **R**, it can be expanded as a Fourier series in the surface reciprocal lattice vectors $G_{m,n}$:

$$V(\mathbf{r}) = V_0(z) + \sum_{G_{m,n} \neq 0} V_G(z)\exp(i\mathbf{G}\cdot\mathbf{R}) , \qquad (1)$$

where $\mathbf{r} = (\mathbf{R},z)$ is the position of the impinging atom. (Boldface refers to vector quantities, capitals refer to components parallel to the surface.)

It was originally hoped that the elastic scattering of He from ordered rare gas surfaces would yield detailed information about the nature of the multibody expansion of the He-surface potential; i.e., which higher order terms should be included in the potential expansion, and about the magnitude of these terms. This premise was implicitly based upon the assumption that the He–RG pair potentials {RG = Ar,Kr,Xe} were sufficiently refined so that any observed discrepancies between the data and calculations could be attributed to the effects of higher order terms in the potential. Furthermore, several different adsorbed film thicknesses were used in order to assess the substrate's contribution to the overall potential. Here, the utilization of

1,2,3, and 25 layer films allowed the surface–substrate distance to be varied in a controlled manner. The detailed comparisons presented in this paper between selective adsorption data and converged quantum scattering calculations do in fact demonstrate the *extreme* sensitivity that such measurements have to subtle changes in the He–surface potential. It will be shown that the results suggest that further refinements in the He-heavy–rare gas pair potentials may be in order.

Presenting the results of the elastic and inelastic measurements in separate papers is not meant to imply that the two scattering processes are independent. The fact that the surface is vibrating leads to the temperature dependent attenuation of the elastic features. This is usually accounted for by an exponential Debye–Waller factor. Some of the scattered atoms may have even undergone transitions involving both elastic processes. However, the principal information sought from elastic and inelastic scattering was different. In the former, the surface dynamics of the overlayers gave information about the interaction of the physisorbed atoms with each other and the Ag substrate. On the other hand, the elastic scattering measurements provide a direct way of examining the probe particle–surface interaction potential, and the various components that contribute to its construction.

Similar experiments involving light atom scattering from rare gas overlayers physisorbed on graphite have been reported.[9–13] These have been compared, with varying degrees of success, to accurate scattering calculations.[14–17] This paper will proceed in the same vein. Two types of experiments are discussed. The first is diffraction, where the incident polar and azimuthal angles are held constant, and the scattered signal is measured as a function of final scattering angle over a wide range of final angles. The second is selective adsorption, where the specular intensity is tracked as a function of polar and azimuthal angles. Most of the work was done using an 18 meV He beam. In the case of the Xe monolayer, a 68 meV beam was also used. The results of these experiments are then compared with elastic close-coupling calculations, where the contributions of several terms that might contribute to the total He–surface potential are considered.

EXPERIMENTAL

The experimental apparatus has been described in detail elsewhere.[18] Modifications used in these experiments, and the procedures used for growing the ordered overlayers are discussed in our previous papers.[2,3] In this section, the important features will be briefly summarized. The helium beams were produced by a supersonic expansion from an approximately $12 \, \mu m$ diameter pinhole. Two different energies were used. The higher energy beam was approximately 66 meV, with a $\Delta v/v \approx 2.4\%$ FWHM. The lower energy beam was about 18 meV, with a $\Delta v/v \approx 1.3\%$ FWHM, produced by cooling the nozzle with liquid N_2. The energy of the 66 meV beam could be off by as much as 1 meV, while the lower energy beam should be accurate to within better than 0.1 meV. The angular spread of the beam was 0.13°, making a

beam spot diameter at normal incidence of about 0.9 mm at the crystal. The substrate was a 12.5 mm diameter single crystal of Ag, oriented within 0.5° of the (111) face, as verified by Laue x-ray scattering. It was spot welded to a manipulator which had both polar and azimuthal angle adjustments. A ruled circular scale was firmly attached to the crystal manipulator. By observing this scale with a fixed telescope, it was possible to set the azimuthal angle within better than 0.2°. Polar angles could be determined to better than 0.5°. The angular position of the detector could be varied independently of the crystal. The angular acceptance of the detector was 0.67°. A separate beam was used for dosing the crystal with Ar, Kr, or Xe. The size of the dosing beam spot at the crystal was twice that of the He beam. Monolayer growth procedures are given in Ref. 2, and multilayer growth procedures are given in Ref. 3. Coverage was quantitatively confirmed using temperature-programmed thermal desorption spectroscopy.

The incident beam was mechanically modulated by a rotating chopper, spinning at 200 or 250 Hz. It had two large slots positioned 180° apart, each of which allowed the beam to pass 25% of the time. In between the large slots were two narrow slots. A photodiode monitored the openings of the chopper with respect to the beam. By utilizing the differences in the open times of the two sets of slots, it was possible to look at the beam passed by each set separately. The small slots allowed the beam velocity and velocity spread to be
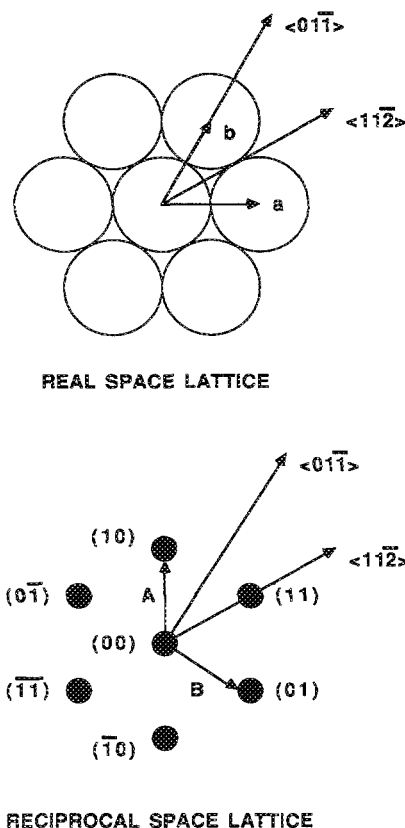

REAL SPACE LATTICE

RECIPROCAL SPACE LATTICE

FIG. 1. Surface geometry for the rare gas overlayers, showing the two symmetry directions used in the experiments. a and b are the unit lattice vectors, A and B are the unit reciprocal lattice vectors.

determined by measuring the time of flight of the He beam. This is described in Ref. 2. The larger slots were used for the experiments described in this paper.

Diffraction runs were done by keeping the incident polar and azimuthal angles fixed, and varying the position of the detector in discrete intervals of 0.25°. At each final angle, data was digitally collected for about 6 s using two Camac controlled scalars, and the data stored by a PDP-11/20 computer. One scalar collected signal when the chopper was closed. The latter represented the background in the detector, and was subtracted from the signal collected when the chopper was open to give the true scattered intensity. The same arrangement could be used to measure the intensity of the incident beam, by lowering the crystal and moving the detector directly into the path of the beam.

Selective adsorption experiments were done by monitoring the scattered intensity at the specular angle, at ~0.2° increments of polar angle, for a fixed azimuthal angle. The signal was amplified by a Keithley electrometer. The output of the electrometer was then demodulated by a lock-in amplifier whose reference signal was from the photodiode monitoring the chopper. Finally, the demondulated signal was digitized by a voltmeter, and transferred to the computer.

Diffraction

Figure 1 shows the real space and reciprocal space lattices for the rare gas over layers, while Figs. 2–8 show diffraction spectra for the rare gas surfaces studied. Elastic diffraction peaks occur at polar angles determined from the conservation of parallel crystal momentum, $K_f = K_i + G_{m,n}$. The intensities are related to the gas–surface interaction potential. Before proceeding with a quanti-

tative analysis of the elastic scattering, a qualitative look at the spectra is in order.

The relatively narrow peaks and the low background, at least in the case of the 18 meV beam, are indicative of the well-ordered nature of all of these surfaces. The Ag(111)
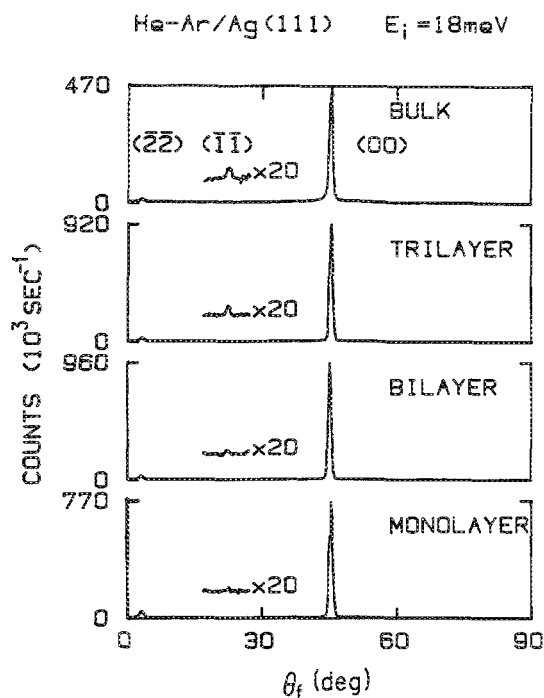

FIG. 3. Experimental He diffraction spectra along the $\langle 11\bar{2} \rangle$ azimuth for the Kr overlayers $\Theta_i = 45°$, and $E_i = 18$ meV. The bulk coverage was 39 layers. Experimental conditions and diffraction probabilities are given in Table II.

FIG. 2. Experimental He diffraction spectra along the $\langle 11\bar{2} \rangle$ azimuth for the Ar overlayers $\Theta_i = 45°$ and $E_i = 18$ meV. The bulk coverage was 35 layers. Experimental conditions and diffraction probabilities are given in Table I.
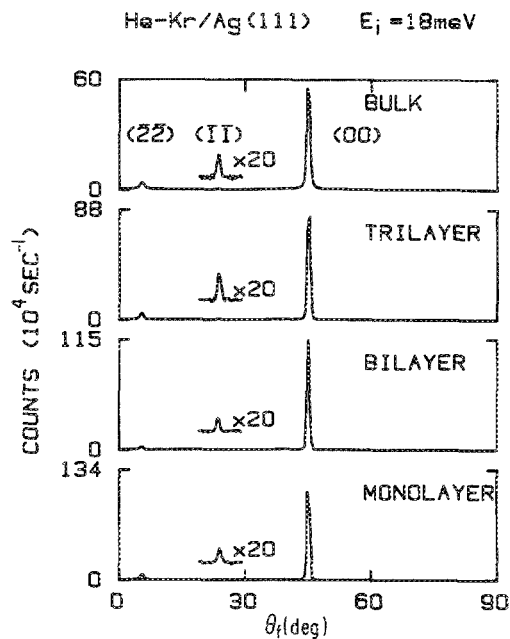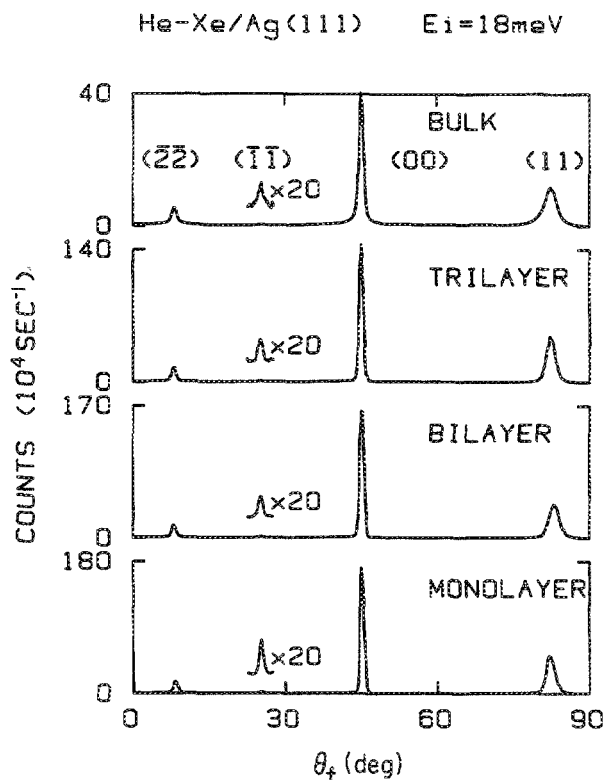

FIG. 4. Experimental He diffraction spectra along the $\langle 11\bar{2} \rangle$ azimuth for the Xe overlayers $\Theta_i = 45°$ and $E_i = 18$ meV. The bulk coverage was about 25 layers. Experimental conditions and diffraction probabilities are given in Table III.
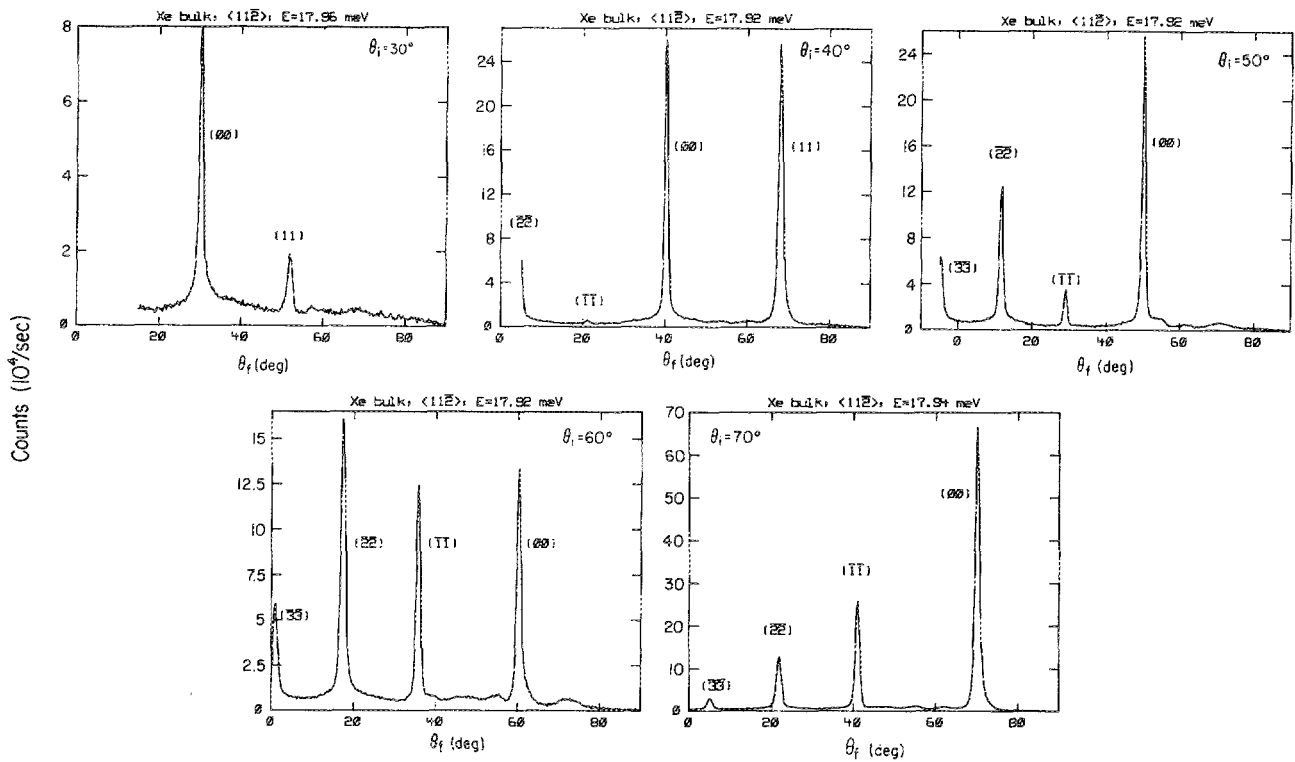
FIG. 5. Experimental He diffraction spectra along the ⟨11$\bar{2}$⟩ azimuth for 25 layers of Xe, at incident angles of 30°, 40°, 50°, 60°, and 70°, and with $E_i = 18$ meV. Experimental conditions and diffraction probabilities are given in Table III.

FIG. 6. Experimental He diffraction spectra along the ⟨01$\bar{1}$⟩ azimuth for 25 layers of Xe, at incident angles of 40°, 50°, 60°, and 70°, and with $E_i = 18$ meV. Experimental conditions and diffraction probabilities are given in Table III.
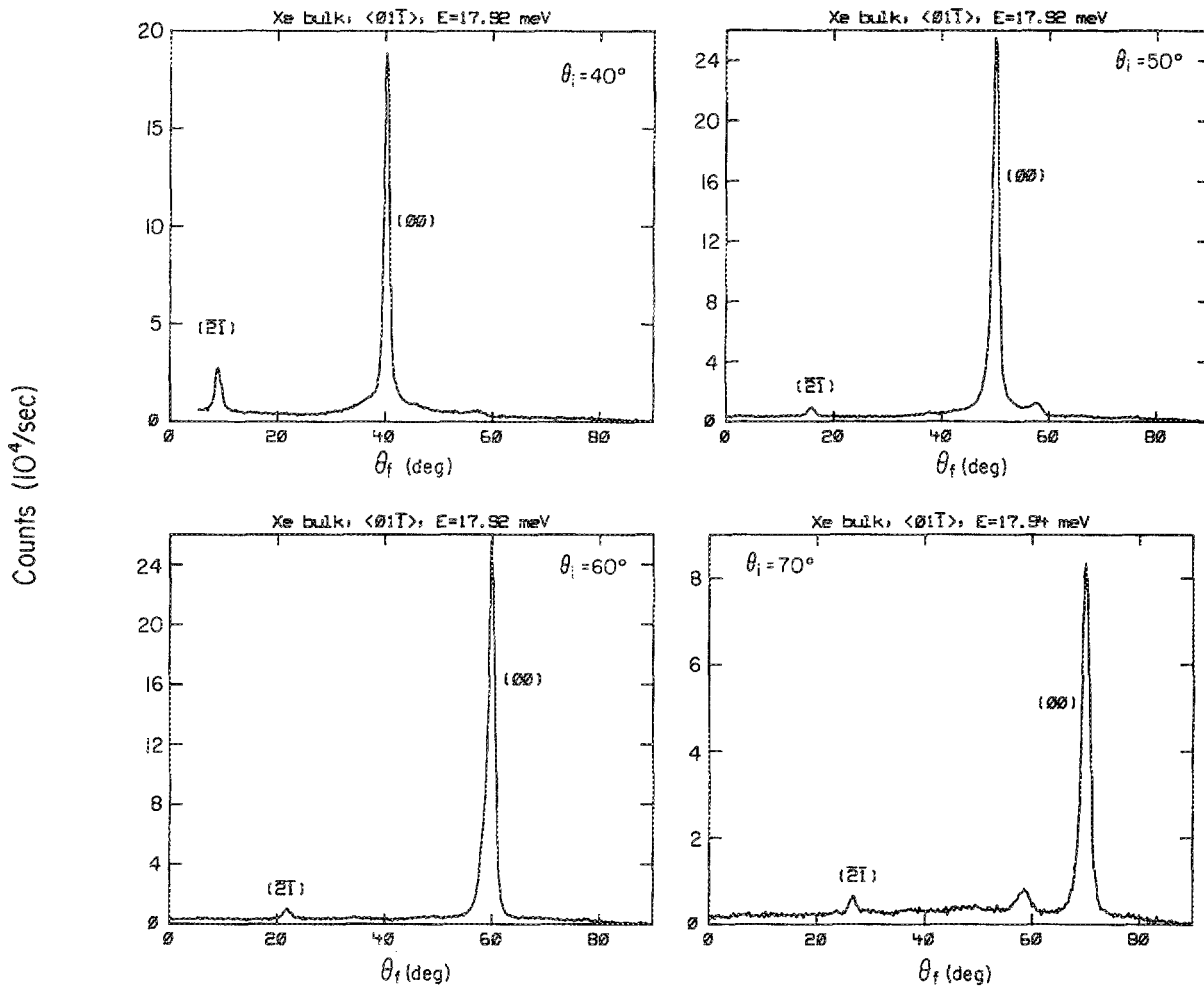
FIG. 7. Experimental He diffraction spectra along the $\langle 11\bar{2} \rangle$ azimuth for monolayer Xe, $E_i = 66.3$ meV, at incident angles of 30°, 40°, 50°, 60°, 70°, and 80°. Experimental conditions and diffraction probabilities are given in Table IV.

substrate certainly consisted of randomly stepped terraces. The overlayers, particularly the monolayer, are expected to reflect this underlying structure. The widths of the diffraction peaks are larger than the instrument function, as is the width of the specular peak when scattering from the clean Ag crystal, an indication that the surface consists of finitely sized islands.[19] The dimensions of these islands determines the coherence length of the surface.

Evidence that monolayer Xe is not flat on the scale of several lattice constants shows up at glancing incidence an-

FIG. 8. Experimental He diffraction spectra along the $\langle 01\bar{1} \rangle$ azimuth for monolayer Xe, $E_i = 66.3$ meV, at incident angles of 30°, 40°, 50°, 60°, 70°, and 80°. Experimental conditions and diffraction probabilities are given in Table IV.

gles. The specular peaks for the high energy beam at $\Theta_i = 80°$ are rather broad at the base, and could be composed of several merged peaks. As mentioned, a finite coherence length will show up as a broadening of the specular, particularly at glancing incident angles. It is possible that the effect is also partially due to a superlattice structure, where there is some additional long wavelength periodicity in the way that the atoms are ordered. The result will be small elastic features on either side of the specular, due to diffraction from the superlattice. There are other geometric effects at very glancing angles. The crystal is sufficiently large such that, even at $\theta_i = 80°$, the entire incident beam will hit the Ag crystal when it is nearly centered. The dosing beam spot size is twice as large as the incident beam, and final dosing was done at $\Theta_i = 70°$. However, at $\Theta_i = 80°$, this means that the incident beam nearly covers the entire length of the rare gas covered area along the scattering direction, assuming that there is no spreading of the dosed rare gas at the edges of the dosing region. Since the Ag has close to 90% specular scattering at the surface temperatures used, if the He beam hits even a small area of bare metal, there will be a large increase in the specular scattering. In fact, the data taken at $\Theta_i = 80°$ shows a very large specular reflection, which could be due to this effect.

Possible evidence for a superlattice structure clearly shows up in one diffraction spectrum, that of a Xe monolayer taken at $\Theta_i = 70°$ with a 66 meV beam. The specular peak has satellite peaks, one at $\Theta_f = 68°$ and a smaller one on the other side of the specular. We do not know if the scattering at these angles is elastic. If it is, their presence might indicate a superlattice periodicity of about 45 Å. We also note that, unlike the Xe overlayers physisorbed on Pt(111),[20] the overlayers of rare gases physisorbed on Ag(111) are azimuthally aligned with the substrate. This latter observation is also in agreement with the experiments of Webb and co-workers.[21,22]

It should be noted that spectra taken at $\Theta_i = 70°$ with a 66 meV beam were used to compare various Xe monolayers when we were originally developing our dosing procedure. By varying the dosing time and angle, as well as the surface temperature and annealing procedures, the size and position of the satellite peaks could be changed. The final dosing procedure was decided for the case where these peaks were small, and the intensities of the elastic features were reproducible.

There is also He scattering at final angles between the kinematically allowed elastic diffraction peaks, particularly for the higher energy beam. Some of this is incoherent elastic scattering from crystal defects. However, much of it is due to inelastic scattering. It is also apparent that this scattering does not have a simple cosine intensity distribution. We have not made an attempt to interpret all of the scattering processes that lead to the intensity variations in this "background." There is one striking feature in the spectra taken with an 18 meV beam scattering from 25 layers of Xe along the $\langle 01\bar{1}\rangle$ azimuth. At $\Theta_i = 40°$, 50°, and 70° there is a broad maximum in the intensity that shows up at a final angle slightly less than 60°. Though the intensity is variable with incident angle, the final angle is almost the same. Lilien-

kamp[23] observed a feature with similar behavior in the scattering of He from LiF(001). The scan curve

$$E_f = \frac{\hbar^2 K^2}{2m \sin^2(\Theta_f)} \qquad (2)$$

was nearly parallel to the parabola for selectively adsorbed atoms,

$$E_f = \frac{\hbar^2 K^2}{2m} - |E_n|, \qquad (3)$$

over a wide range of final energies for the $v = 0$ bound state, with a difference in parallel momentum close to an in-plane reciprocal lattice vector. He atoms appearing at this "magic" final angle had undergone adsorption phonon creation processes, followed by selective emission, in this case diffraction by a unit reciprocal lattice vector.

A process like this, in which the first step involves interaction with a phonon, seems the only reasonable way to explain a feature whose position is independent of the incident angle. No time-of-flight spectra were taken at his angle, so the final energies are unknown. Using the levels calculated for the Maitland–Smith He–Xe pair potential with a three-body He–Xe–Xe Axilrod–Teller–Muto interaction (the Ag substrate is too far from the surface to have much effect), the difference in the parabolas was not an in-plane reciprocal lattice vector. The $v = 0$ state, with $E_0 = -4.34$ meV, was the nearest to being parallel to the scan curve for reasonable energy loss, but the difference was close to 1.67 Å^{-1}, which is the length of a unit reciprocal lattice vector. So, the mechanism might explain a feature near 58° along the $\langle 11\bar{2}\rangle$ azimuth, but not along the $\langle 01\bar{1}\rangle$ azimuth.

A simulation program was used to extract the elastic scattering probabilities. The first step was to fit the elastic features. This was done with a nonlinear least-squares fitting routine, using a sum of two Gaussians of the form

$$I = I_0 \exp\left[\left(\frac{\Theta_f - \Theta_0}{\Theta_w}\right)^2\right], \qquad (4)$$

where Θ_0 is the angular position maximum and Θ_w is the width. One Gaussian represented the elastic feature, and the other modeled the background by fitting the scattered intensity on either side of the peak. This symmetric function gave good fits to many of the peaks. In some cases, there is some asymmetry to the features. For instance, with an 18 meV beam, the specular peak for scattering from bulk Xe at $\Theta_i = 60°$ along the $\langle 01\bar{1}\rangle$ azimuth has a wing at smaller final angles. This is due to a large change in scattering intensity near this angle caused by a selective adsorption resonance, as shown in Fig. 10(b). Also, for nonspecular diffraction peaks at near glancing final angles, the Bragg condition will introduce some asymmetry. To treat asymmetry, the fitting function was expanded as a series of Hermite polynomials.

The specular intensity was checked before and after each diffraction run to monitor surface cleanliness. In most cases, the change was only a few percent. However, the results taken along the $\langle 01\bar{1}\rangle$ azimuth with the higher energy beam showed much higher attenuations over the course of a run, as much as 25%. In this case, the intensity at the peak of

the specular and the diffraction peaks were checked at periodic intervals during the course of an experiment. These results were then used to time normalize the intensities. It is also important to note that, as mentioned previously,[2] Xe monolayers grown at the beginning of these series of experiments did not diffract as well as those grown towards the end, though the ratios of the intensities of the diffraction peaks were similar. The relative intensities of diffraction peaks within a spectrum are a better comparison than the comparision of intensities between spectra.

The intensities determined were then compared with the results of the simulation program. Time-of-flight measurements gave the velocity distribution of the incident beam. This was convoluted with the gate function of the mechanical chopper, the angular spread of the beam, the beam spot size at the crystal, and the detector resolution function. The final angle for the scattering was determined from the kinematical conditions, using lattice constants determined from the angular positions of the diffraction peaks. This simulation was done over a range of final angles to build up a model of the diffraction peak to compare with the experimental data, assuming that the scattering into any particular diffraction peak has unit probability. Its intensity was calibrated by comparison with an angular scan of the straight-through beam. Thus, the ratio of integrated intensities between the experiment and the simulation gave the average scattering probability I_G/I_0 for the observed peak. This latter point is important, as the scattering probability is not necessarily constant even over the narrow velocity distribution of our beam. The results are shown in Tables I–IV.

The angular width of the simulation was close to that of the experimental measurements for the straight-through beam. For the elastic diffraction peaks, it was consistently too narrow. We attribute this to the coherence length of the surface. As previously mentioned, the surface is probably composed of finite sized islands, and the size of these islands is the coherence length. In one dimension, a monoenergetic beam would approximately have a shape determined by the relation[24]

$$I = \frac{\sin^2(0.5N\Delta\mathbf{K}\cdot\mathbf{a})}{\sin^2(0.5\Delta\mathbf{K}\cdot\mathbf{a})} . \tag{5}$$

N is the number of atoms in the length of an ordered island and $\mathbf{a}$ is a real space lattice vector. In reciprocal space this function has an approximately Gaussian central shape, with N-2 small sidebands. The FWHM of the central Gaussian is approximately $5.54/L_c$, where L_c is the coherence length. Since the fits to the data and simulations are also Gaussian,

$$\Delta\Theta_w = (\Delta\Theta_{\mathrm{exp}}^2 - \Delta\Theta_{\mathrm{inst}}^2)^{0.5} \approx \frac{5.54}{L_c k \cos\Theta_f} , \tag{6}$$

where $\Delta\Theta_w$ is the FWHM of the incoherent broadening, $\Delta\Theta_{\mathrm{exp}}$ is the FWHM of the experimentally measured peak, and $\Delta\Theta_{\mathrm{inst}}$ is the FWHM of the instrument function. There is some discrepancy in the measurement of the coherence length depending upon the beam. The specular at $\Theta_i = 50°$ gave a coherence length for the Ag substrate of 75 Å, and a coherence length for a Xe monolayer of 70 Å. With an 18 meV beam, the coherence lengths determined for the overlayers were in the neighborhood of 120 Å. We are not sure where this discrepancy comes from, but it seems reasonable to assume a coherence length of ∼100 Å.

TABLE I. Elastic scattering probabilities for the Ar overlayers $E_i = 18$ meV. The numbers in parentheses are the standard deviation and number of measurements, in this case done on the same surface.

Θ_i (deg)	Diffraction rod	Probability $I_G/I_0(\%)$	E_i (meV)	T_s (K)
		Monolayer, $\langle 11\bar{2}\rangle$		
45	(00)	1.12	18.02	21
	$(\bar{1}\bar{1})$	1.5×10^{-3}		
	$(\bar{2}\bar{2})$	$9.1\times10^{-2}(1.6\times10^{-2},3)$		
		Bilayer, $\langle 11\bar{2}\rangle$		
45	(00)	1.24	18.03	21
	$(\bar{1}\bar{1})$	2.9×10^{-3}		
	$(\bar{2}\bar{2})$	$5.5\times10^{-2}(6\times10^{-3},3)$		
		Trilayer, $\langle 11\bar{2}\rangle$		
45	(00)	1.30	18.03	21
	$(\bar{1}\bar{1})$	5.4×10^{-3}		
	$(\bar{2}\bar{2})$	$4.7\times10^{-2}(2\times10^{-3},3)$		
		35 layers, $\langle 11\bar{2}\rangle$		
45	(00)	5.88×10^{-1}	18.03	21
	$(\bar{1}\bar{1})$	3.8×10^{-3}		
	$(\bar{2}\bar{2})$	$2.1\times10^{-2}(6\times10^{-3},2)$		

TABLE II. Elastic scattering probabilities for the Kr overlayers $E_i = 18$ meV. The numbers in parentheses are the standard deviation and number of measurements, in this case done on the same surface.

Θ_i (deg)	Diffraction rod	Probability $I_G/I_0(\%)$	E_i (meV)	T_s (K)
		Monolayer, $\langle 11\bar{2}\rangle$		
45	(00)	1.94	18.05	22
	$(\bar{1}\bar{1})$	1.6×10^{-2}		
	$(\bar{2}\bar{2})$	1.20×10^{-1}		
		Bilayer, $\langle 11\bar{2}\rangle$		
45	(00)	1.65	18.05	22
	$(\bar{1}\bar{1})$	1.2×10^{-2}		
	$(\bar{2}\bar{2})$	$6.0\times10^{-2}(1\times10^{-2},2)$		
		Trilayer, $\langle 11\bar{2}\rangle$		
45	(00)	1.34	18.05	22
	$(\bar{1}\bar{1})$	1.9×10^{-2}		
	$(\bar{2}\bar{2})$	7.7×10^{-2}		
		39 layers, $\langle 11\bar{2}\rangle$		
45	(00)	8.59×10^{-1}	18.11	22
	$(\bar{1}\bar{1})$	1.0×10^{-2}		
	$(\bar{2}\bar{2})$	6.4×10^{-2}		

TABLE III. Elastic scattering probabilities for the Xe overlayers $E_i = 18$ meV. The numbers in parentheses are the standard deviation and number of measurements done, in this case for different surfaces.

Θ_i (deg)	Diffraction rod	Probability $I_G/I_0(\%)$	E_i (meV)	T_s (K)
		Monolayer, $\langle 11\bar{2}\rangle$		
45	(11)	1.02	18.05	22
	(00)	1.59		
	$(\bar{1}\bar{1})$	2.0×10^{-2}		
	$(\bar{2}\bar{2})$	1.56×10^{-1}		
50	(00)	6.26×10^{-1}	17.93	25
	$(\bar{1}\bar{1})$	1.7×10^{-2}		
	$(\bar{2}\bar{2})$	5.9×10^{-2}		
70	(00)	2.17×10^{-1}	17.93	24
	$(\bar{1}\bar{1})$	1.15×10^{-1}		
	$(\bar{2}\bar{2})$	6.2×10^{-2}		
	$(\bar{3}\bar{3})$	1.5×10^{-2}		
		Bilayer, $\langle 11\bar{2}\rangle$		
45	(11)	1.10	18.05	22
	(00)	1.69		
	$(\bar{1}\bar{1})$	1.3×10^{-2}		
	$(\bar{2}\bar{2})$	1.51×10^{-1}		
		Trilayer, $\langle 11\bar{2}\rangle$		
45	(11)	1.12	18.05	22
	(00)	1.45		
	$(\bar{1}\bar{1})$	1.3×10^{-2}		
	$(\bar{2}\bar{2})$	1.51×10^{-1}		
		25 layers, $\langle 11\bar{2}\rangle$		
30	(11)	3.2×10^{-2}	17.96	24
	(00)	1.30×10^{-1}		
40	(11)	4.10×10^{-1}	17.92	24
	(00)	3.22×10^{-1}		
	$(\bar{1}\bar{1})$	3.8×10^{-3}		
45	(11)	3.52×10^{-1}	17.92	24
	(00)	5.14×10^{-1}		
	$(\bar{1}\bar{1})$	3.6×10^{-3}		
	$(\bar{2}\bar{2})$	7.5×10^{-2}		
50	(00)	3.31×10^{-1}	17.92	24
	$(\bar{1}\bar{1})$	4.3×10^{-2}		
	$(\bar{2}\bar{2})$	1.79×10^{-1}		
	$(\bar{3}\bar{3})$	$\sim 9\times10^{-2}$		
60	(00)	$1.99\times10^{-1}(1.6\times10^{-2},2)$	17.94	24
	$(\bar{1}\bar{1})$	$1.66\times10^{-1}(1.4\times10^{-2},3)$		
	$(\bar{2}\bar{2})$	$2.49\times10^{-1}(2.8\times10^{-2},2)$		
	$(\bar{3}\bar{3})$	$9.6\times10^{-2}(3.6\times10^{-3},2)$		
70	(00)	1.11	17.94	24
	$(\bar{1}\bar{1})$	4.17×10^{-1}		
	$(\bar{2}\bar{2})$	2.32×10^{-1}		
	$(\bar{3}\bar{3})$	5.8×10^{-2}		
		25 layers, $\langle 01\bar{1}\rangle$		
40	(00)	2.74×10^{-1}	17.92	24
	$(\bar{2}1)$	3.6×10^{-2}		
50	(00)	$4.43\times10^{-1}(2.1\times10^{-2},2)$	17.93	24
	$(\bar{2}1)$	1.0×10^{-2}		
60	(00)	$5.23\times10^{-1}(5.5\times10^{-2},3)$	17.93	24
	$(\bar{2}1)$	$1.9\times10^{-2}(1\times10^{-3},2)$		
70	(00)	1.89×10^{-1}	17.94	24
	$(\bar{2}1)$	6.3×10^{-3}		

TABLE IV. Elastic scattering probabilities for Xe monolayers $E_i = 66.3$ meV. The numbers in parentheses are the standard deviation and number of measurements for different surfaces, except for $\Theta_i = 70°$ along the $\langle 11\bar{2}\rangle$ azimuth, where more than one measurement was made off of each of the surfaces.

Θ_i (deg)	Diffraction rod	Probability $I_G/I_0(\%)$	T_s (K)
		Monolayer, $\langle 11\bar{2}\rangle$	
30	(33)	3.3×10^{-2}	24
	(22)	8.6×10^{-3}	
	(11)	1.6×10^{-2}	
	(00)	4.6×10^{-3}	
	$(\bar{1}\bar{1})$	2.5×10^{-3}	
40	(22)	$9.3\times10^{-2}(5\times10^{-4},2)$	24
	(11)	$3.4\times10^{-2}(3\times10^{-3},2)$	
	(00)	$3.0\times10^{-2}(5\times10^{-3},2)$	
	$(\bar{1}\bar{1})$	$1.3\times10^{-2}(6\times10^{-4},2)$	
	$(\bar{2}\bar{2})$	$8.7\times10^{-3}(4\times10^{-4},2)$	
	$(\bar{3}\bar{3})$	$1.5\times10^{-3}(2\times10^{-4},2)$	
50	(11)	8.2×10^{-2}	23
	(00)	5.8×10^{-2}	
	$(\bar{1}\bar{1})$	4.0×10^{-2}	
	$(\bar{2}\bar{2})$	1.2×10^{-2}	
	$(\bar{3}\bar{3})$	1.7×10^{-3}	
	$(\bar{4}\bar{4})$	5.1×10^{-3}	
	$(\bar{5}\bar{5})$	2.8×10^{-3}	
60	(00)	8.4×10^{-2}	23
	$(\bar{1}\bar{1})$	5.5×10^{-2}	
	$(\bar{2}\bar{2})$	2.1×10^{-2}	
	$(\bar{3}\bar{3})$	1.7×10^{-2}	
	$(\bar{4}\bar{4})$	1.1×10^{-2}	
	$(\bar{5}\bar{5})$	2.3×10^{-3}	
70	(00)	$1.30\times10^{-1}(9\times10^{-3},10)$	23–24
	$(\bar{1}\bar{1})$	$3.40\times10^{-1}(4.6\times10^{-2},9)$	
	$(\bar{2}\bar{2})$	1.23×10^{-1}	
	$(\bar{3}\bar{3})$	4.3×10^{-2}	
	$(\bar{4}\bar{4})$	1.3×10^{-2}	
	$(\bar{5}\bar{5})$	$<1\times10^{-3}$	
	$(\bar{6}\bar{6})$	$<1\times10^{-3}$	
80	(00)	3.4	23
	$(\bar{1}\bar{1})$	7.90×10^{-1}	
	$(\bar{2}\bar{2})$	1.57×10^{-1}	
	$(\bar{3}\bar{3})$	3.1×10^{-2}	
	$(\bar{4}\bar{4})$	4.4×10^{-3}	
	$(\bar{5}\bar{5})$	$<1\times10^{-3}$	
	$(\bar{6}\bar{6})$	$<1\times10^{-3}$	
		Monolayer, $\langle 01\bar{1}\rangle$	
30	(21)	3.5×10^{-2}	24
	(00)	2.1×10^{-3}	
	$(\bar{2}\bar{1})$	1.8×10^{-2}	
40	(21)	8.5×10^{-2}	24
	(00)	6.0×10^{-2}	
	$(\bar{2}\bar{1})$	1.9×10^{-2}	
	$(\bar{4}\bar{2})$	8.6×10^{-3}	
50	(00)	6.5×10^{-2}	24
	$(\bar{2}\bar{1})$	3.2×10^{-2}	
	$(\bar{4}\bar{2})$	1.0×10^{-2}	
60	(00)	4.21×10^{-1}	23
	$(\bar{2}\bar{1})$	8.9×10^{-2}	
	$(\bar{4}\bar{2})$	5.6×10^{-3}	
	$(\bar{6}\bar{3})$	$<1\times10^{-3}$	
70	(00)	$1.10(2\times10^{-2},4)$	23–24
	$(\bar{2}\bar{1})$	$5.6\times10^{-2}(9\times10^{-3},4)$	
	$(\bar{4}\bar{2})$	1×10^{-3}	
	$(\bar{6}\bar{3})$	$<1\times10^{-3}$	
80	(00)	1.2	24
	$(\bar{2}\bar{1})$	2.7×10^{-2}	
	$(\bar{4}\bar{2})$	$<1\times10^{-3}$	
	$(\bar{6}\bar{3})$	$<1\times10^{-3}$	

Selective adsorption

Figures 9–12 show the specularly scattered He intensity as a function of incident angle for the three rare gases. The many peaks and dips in the spectra are the signature of selective adsorption resonances. To zeroth order, the specular intensity will change when the incident conditions are right for the He atoms to make a transition to a state where they are bound to the surface in the perpendicular direction, and free translating parallel to it. In the case of elastic transitions, this free atom approximation predicts that selective adsorption will occur when

$$k_i^2 - \frac{2mE_n}{\hbar^2} = (\mathbf{K}_i + \mathbf{G}_{m,n})^2, \qquad (7)$$

where m is the mass of a He atom and E_n is a level of the laterally averaged potential. This relation is derived from the conservation of parallel crystal momentum and the conservation of energy. The adsorbed state has a very short lifetime; the atom is quickly desorbed either by an elastic transition into some allowed diffraction channel, or scattered by an inelastic transition. The result will be a series of discrete features in the spectra, either maxima or minima, occurring at angles predicted by Eq. (7).

It should be mentioned that there are at least two other possible reasons for these features. Some may be due to thresholds. These occur at angles where formerly closed diffraction channels become open, or vice versa. If the He has (had) a high probability of scattering into the newly open (closed) channel, there can be a large change in the intensity of the specular scattering. In the absence of selective adsorption resonances, changes in the specular intensity due to thresholds would be steps rather than sharp features. These angles can be calculated from the conservation of parallel crystal momentum $\mathbf{K}_f = \mathbf{K}_i + \mathbf{G}_{m,n}$. The positions of threshold features should give values of $E_n \approx 0$ when using the free-atom approximation. The second consideration is the finite size of the rare gas islands. If the islands occur as a stepped structure, there can be constructive and destructive interference for scattering from the steps. Considering the size of the islands, ~ 100 Å, the intensity variation should be small.[19] Also, assuming the islands vary in height by one or two rare gas atoms, we note that there is no correlation between the observed structure and predicted angles of constructive and destructive interference. This is further shown by the fact that features in the spectra move when going from one to many layers of the same rare gas.

The free-atom approximation ignores the higher order Fourier components ($V_G, \mathbf{G}_{m,n} \neq 0$) of the potential. For a highly corrugated surface, where some periodic components of the potential are significant with respect to V_0, the free-atom approximation is not strictly valid. This is especially true in regions of $\mathbf{K}$ space where there are zero order degeneracies, which are lifted by coupling due to the higher order Fourier coefficients.[25] The resulting selective adsorption features do not necessarily occur exactly at the positions predicted by the free-atom approximation. The specular intensity experiments were performed at only one or two azimuthal angles for most of the surfaces, and these were in high sym-
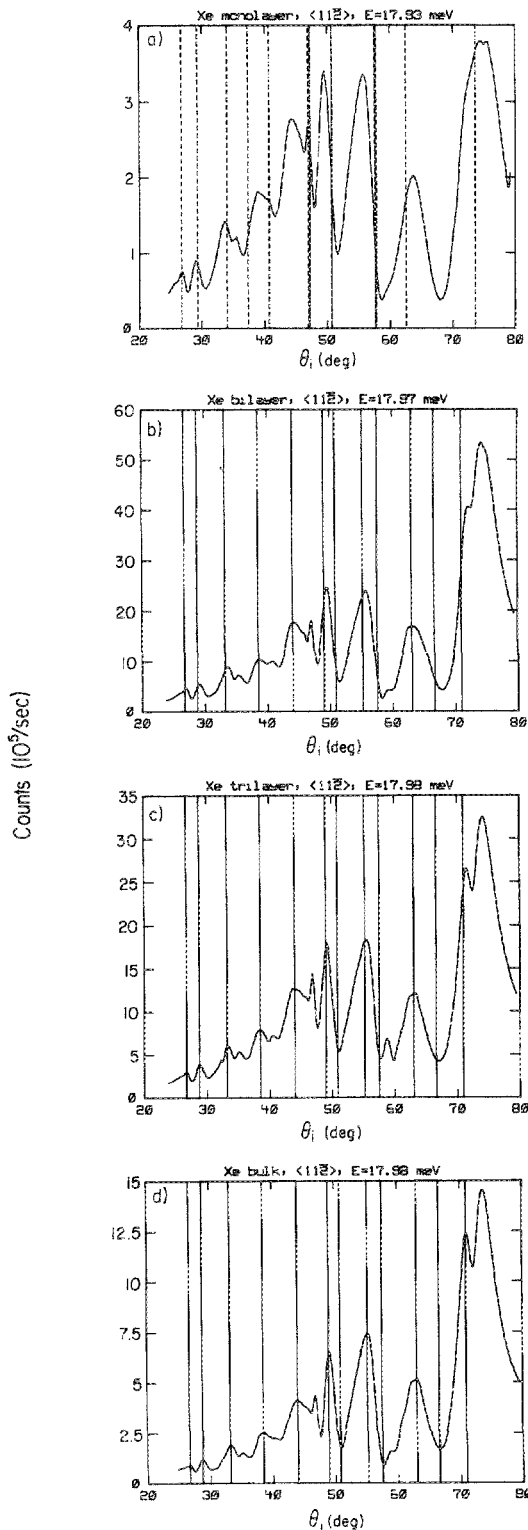

FIG. 9. Selective adsorption spectra along the $\langle 11\bar{2} \rangle$ azimuth for the Xe overlayers. Surface temperatures were 24 K for the monolayer, and 25 K for the other overlayers. Bulk corresponds to 25 layers. The vertical lines on the monolayer spectrum correspond to the angular positions of the resonances plotted in Fig. 13. These are, from left to right, 2–22 (i.e., the $v = 2$ level coupled with G_{22}), 1–22, 0–22, 2–20, 1–20, the nearly overlapping 0–20 and 2–11, 1–11, the nearly overlapping 0–11 and 2–01 and 2–10, the overlapping 1–01 and 1–10, and the overlapping 0–01 and 0–10. The solid vertical lines on the multilayer spectra are drawn to demonstrate how the positions of some features move with increasing overlayer thickness. The monolayer spectrum is not included in this comparison due to its larger lattice constant. In these spectra, as well as the other selective adsorption spectra shown, experimental conditions varied, so that absolute intensities are not comparable between spectra.
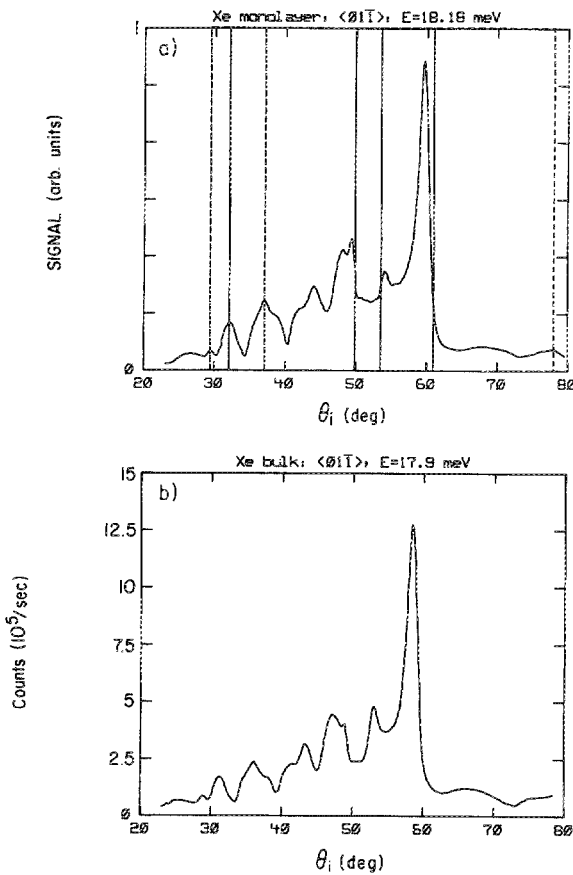
FIG. 10. Selective adsorption spectra along the $\langle 01\bar{1}\rangle$ azimuth for monolayer and 25 layer Xe. Surface temperatures were 25 K for the monolayer, and 23 K for the bulk. The vertical lines on the monolayer spectrum correspond to the angular positions of the resonances plotted in Fig. 13. From left to right, these are the overlapping 2–22 and 2–20, the overlapping 1–22 and 1–20, the overlapping 0–22 and 0–20, the overlapping 2–11 and 2–10, the overlapping 1–11 and 1–10, the overlapping 0–11 and 0–10, and 2–01.
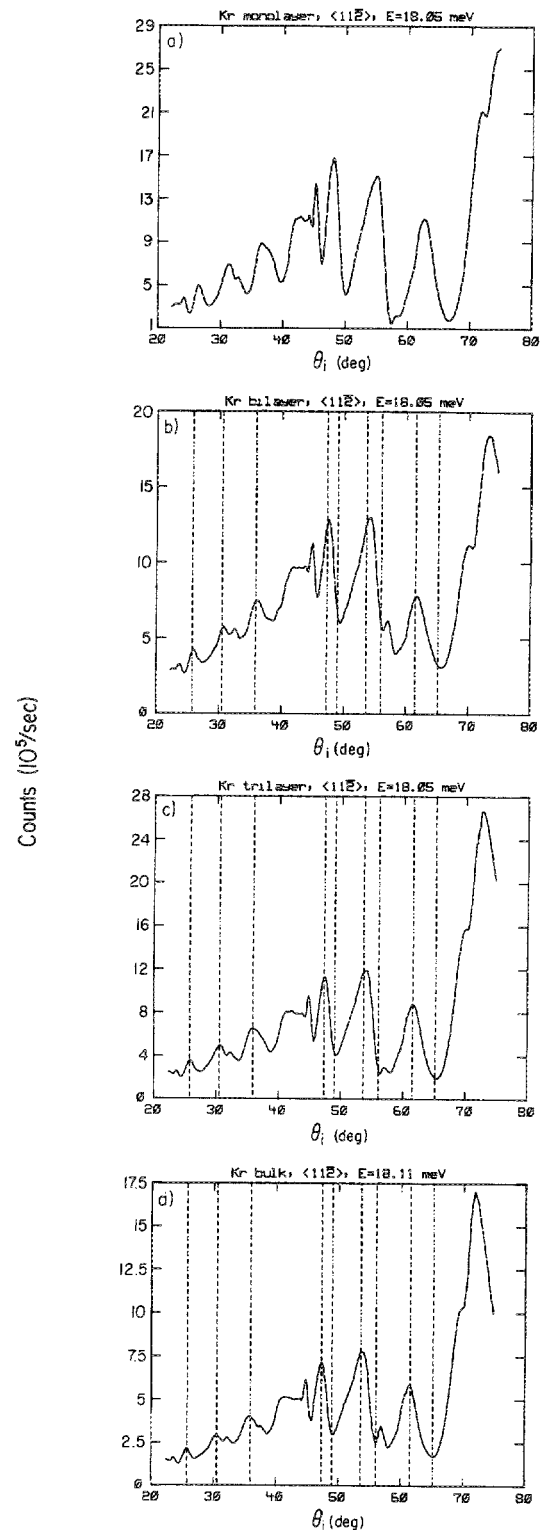

FIG. 11. Selective adsorption spectra along the $\langle 11\bar{2}\rangle$ azimuth for the Kr overlayers. Surface temperature was 22 K. Bulk corresponds to 40 layers. Dashed lines on the multilayer spectra are drawn to show how some of the features move with increasing overlayer thickness. The monolayer spectrum is not included in this comparison due to its larger lattice constant.

metry directions, so that there are many possible curve crossings. Therefore, using the free-atom approximation will probably not be valid. Determining information about the He–surface interaction was done by comparison with close-coupling calculations presented in a later section.

There is a possible way around this dilemma. Spectra can be taken at several different values of both polar and azimuthal angle. The free-atom approximation predicts that when plotted in $\mathbf{K}_x$–$\mathbf{K}_y$ space, the positions of the features will form circles of radii $(E_i + E_n)^{1/2}$ centered at $-\mathbf{G}_{m,n}$. The idea is that there will be regions in reciprocal space that are far from zero order degeneracies, and the zero order theory will sometimes be a good approximation. One problem is that there is no *a priori* way to know the baseline position, so there is no direct way to determine whether it is the maxima or minima that correspond to the selective adsorption resonances. There are general rules for determining whether features should be maxima or minima,[26,27] but it is not clear that they are completely valid for either highly corrugated or very "soft" (inelastic) surfaces.

Only for the Xe monolayer did we perform experiments over a range of azimuthal angles. These were taken in 2° increments from the $\langle 11\bar{2}\rangle$ direction towards the $\langle 01\bar{1}\rangle$ di-

rection, covering all 30° of arc using the 18 meV beam, and 22° of arc using the 67 meV beam. The polar angle at which prominent features occurred was determined, and the free-atom approximation used to determine all the values of E_n for each feature when coupled to reasonable values of $\mathbf{G}_{m,n}$.

FIG. 12. Selective adsorption spectra along the $\langle 11\bar{2} \rangle$ azimuth for the Ar overlayers. Surface temperatures were 21 K. Bulk corresponds to 35 layers. Dashed lines on the multilayer spectra are drawn to show how some of the features move with increasing overlayer thickness. The monolayer spectrum is not included in this comparison due to its larger lattice constant.

FIG. 13. K_x–K_y plot of the specular intensity maxima which occurred in the selective adsorption experiments which used an 18 meV beam. The arcs are the positions of resonances, using the free-atom approximation, for the three energy levels, and coupling G vectors determined (see the text). Solid arcs used E_0, dash–dot arcs used E_1, and dashed arcs used E_2.

The resulting energy levels were plotted as a histogram. If any group of features correlated closely with a circle around some G vector, there should be certain values of energy which would show up as maxima in these histograms. This was done independently for the maxima of each selective adsorption run.

In the case of the 18 meV beam, there were no particularly preferred values of E_n found in the histogram of the minima, but there was a strong correlation for three values of E_n when the maxima were examined. Using the averages, these possible values for the levels of the laterally averaged potential are -4.9, -2.2, and -0.7 meV, with an error within 0.2 meV. One problem in interpreting the results is the shrinkage of the monolayer, as mentioned in the monolayer phonon paper.[2] To compensate for this, we used a linear interpolation between the lattice constants determined before and after each spectrum to determine the lattice constant at each point in the spectrum. In any case, most of the shrinkage occurs soon after the monolayer is grown, and most of the spectra were taken from surfaces that were aged enough that the shrinkage was less than 0.2–0.3 Å for a given run. Even if we use just an average of the before and after lattice constants, the results are within the 0.2 meV error bar of the results using the interpolated lattice constant.

The position of the maxima and the resulting arcs using these values of E_n are shown in Fig. 13. One notable result is that these tentative levels correlate with maxima in the spectra. This would appear to disagree with theoretical treatments of elastic selective adsorption. For instance, rule 1 of Wolfe and Weare[26] predicts a minimum in the specular channel for a selective adsorption resonance strongly coupled to the specular and at least one other outgoing diffraction channel. (Approximately, strong coupling means that the various $G_{m,n}$ are separated by a lowest order reciprocal lattice vector.) This condition is met over a wide range of polar angles for selective adsorption resonances coupled to the lowest order G vectors plotted; the (1,1), (1,0), and (0,1).

However, we want to emphasize that the outlined procedure for determining the levels of V_0 is rather speculative for these highly corrugated surfaces and relatively high beam energies. Using the free-atom approximation, the predicted positions of selective adsorption resonances are plotted on the monolayer spectra of Figs. 9(a) and 10(a). At least for these two azimuthal angles, the energy levels determined do not always correspond to maxima in the spectra.

The same procedure was used with the results from the 67 meV beam experiments. There were fewer prominent features in these spectra, so there are less data to plot. We found clear evidence for only four arcs. Two of these arcs gave evidence for coupling to $G_{1,1}$. The features that make up the arc are minima that appeared in all 11 spectra. In Fig. 14, they are the two rather sharp minima between 60° and 65°. The values of E_n are -4.8 and -2.0 meV, with an error of about 0.2 meV. The other two arcs are coupled to $G_{2,2}$. The features that comprise these two arcs can only be clearly seen up to about 14° to 16° from the $\langle 11\bar{2}\rangle$ direction. It is also difficult to decide whether the proper feature is a minimum or maximum. In Fig. 14, the features are the two maxima and associated minima near 48°. The maxima come the closest to lying on a circle, and give values for the E_n of -5.0 and -2.3 meV. Plotting the minima give values that are at least 0.3 meV lower. Again, a more definitive determination of the levels will have to come from a comparison with the close-coupling calculations.

A few qualitative remarks about the spectra are in order. For the spectra taken with an 18 meV beam, it is interesting how similar the spectra appear, particularly for different overlayer thicknesses of the same rare gas. For the multilayers, vertical lines have been drawn on the spectra to show how the angular positions of corresponding features shift in going from two to many layers. This comparison is valid, since the multilayers of a particular rare gas have the same lattice constant. Especially at glancing angles, some of the features shift towards smaller angles as the number of adsorbed layers increases. This is particularly true for a comparison between bilayer and trilayer. A movement to smaller angles indicates that, for the first few layers added, the levels of the He–surface potential become shallower as the surface–substrate distance increases. This is the type of information that can help determine the substrate influence, and help to decide such questions as the Ag reference plane position z_0.

All of the spectra show a generally decreasing intensity as the incident angle approaches the surface normal. This should be partly due to an increased Debye–Waller attenuation. It is also true that the number of open elastic diffraction channels associated with lower order G vectors is larger at more normal angles. Since these will often be the most strongly diffracting channels, they may serve to rob intensity from the specular channel. The results of the close-coupling calculations indicate that there can be strong diffraction even from many higher order G vectors, so this explanation may not be entirely valid. The spectra taken with the higher energy beam show much less prominent structure. Since there is considerably more inelastic scattering with a 67 meV beam, this result is expected.[28-30] The velocity spread for this beam is also larger than that of the 18 meV beam, and this can help to wash out the structure.

Finally, there are two caveats to keep in mind. One is that the intensities of the specular scattering near $\Theta_i = 80°$ may have some contribution from the bare metal surface. Second, there is the problem we had with Cl contamination of the surface. This was most pronounced at the time we were finishing these experiments. Less than 1% Cl on the surface, as determined by Auger spectroscopy, could cause some of the adsorbed rare gas to form islands which were azimuthally misaligned by 30°. This was determined by the appearance of small features in the diffraction spectra, whose angular position corresponded to $\langle 01\bar{1}\rangle$ diffraction rods. Ar seemed to be particularly sensitive to the contamination. Unfortunately, the Auger spectrometer broke down near the completion of the experiments, and small amounts of Cl did not perturb the specular scattering of He from the Ag substrate enough to be a reliable monitor. The Xe results were definitely obtained with a Cl free Ag substrate, and the Kr results were reproducible. Only the Ar results are possibly effected. The monolayer spectrum was taken soon after sputtering, so all of the islands should be properly aligned. The multilayer spectra may have a small number of misaligned islands. This may be the reason for the maxima in the spectra at about 55°. We will return to this point when we examine the close-coupling calculations. However, the fact that the overall appearance of the multilayer spectra is similar to that of the monolayer, and also to the spectra for Kr and Xe would seem to indicate that the number of misaligned islands is small. When the Ag crystal was not sputtered for one or two days, the appearance of the Ar spectra was considerably different.
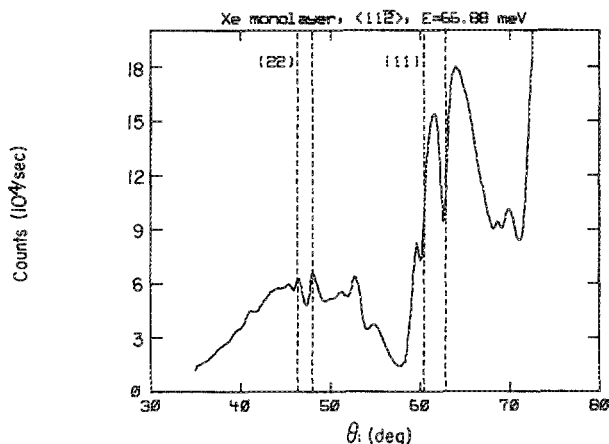
Debye–Waller corrections

The Debye–Waller factor for these rare gas overlayers was discussed previously.[2,3] In this section, some additional information concerning the Xe overlayers will be discussed. Figures 15(a)–15(e) show the intensity of the He scattering at the specular angle for several different incident angles as a function of the surface temperature. Measurements on either side of the specular were made and used to approximate the background to be subtracted from the specular intensities. Included are results for a 66.4 meV beam, and data taken at $\Theta_i = 70°$ with the 18 meV beam. For these data, the simple Debye–Waller approximation used before was not sufficient. It fails badly at glancing angles, $\Theta_i = 70°$ for the 18 meV beam and $\Theta_i = 80°$ for the 66.4 meV beam. An additional dimensionless parameter, $\lambda(k_z)$, was necessary to get

FIG. 14. Selective adsorption spectra along the $\langle 11\bar{2}\rangle$ azimuth for the Xe monolayer $E_i = 66.88$ meV, $T_s = 25$ K. Dashed lines are the positions of resonances in the free-atom approximation, with $E_0 = -4.9$ meV and $E_1 = -2.2$ meV.
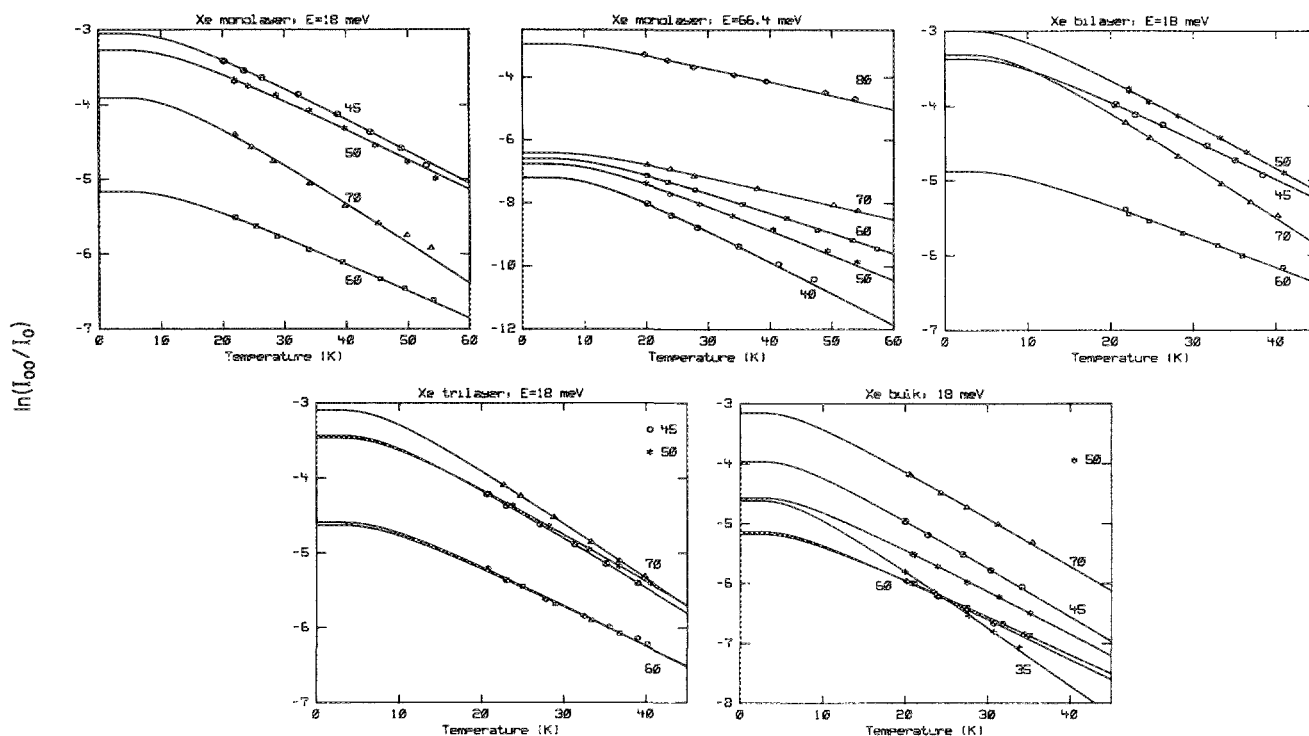
FIG. 15. Plots of $\ln(I_{00}/I_0)$ at various incident angles vs the surface temperature for the Xe overlayers. Solid lines are fits (see the text). For the trilayer and bulk, the points for $\Theta = 60°$ are from two different data sets. The absolute magnitude of the intensities are only approximately correct. This does not effect the slope of the line, which contains the desired information, since the relative magnitudes of the measurements for any particular incident angle are correct.

a closer agreement with the data. The Debye–Waller factor becomes

$$\frac{I_{00}}{I_0} = P_{el} \exp\left[- \lambda^2(k_z)\Delta k_z^2 \langle u_z^2 \rangle \right] . \tag{8}$$

As before, the Beeby correction was used in determining Δk_z,

$$k_z = k \left[\cos^2(\Theta) + \frac{D}{E} \right]^{1/2} , \tag{9}$$

where D is the well depth and E is the incident beam energy. The mean-square value $\langle u_z^2 \rangle$ was determined by

$$\langle u_z^2 \rangle = \left[\frac{\hbar}{2M\omega} \right] \coth\left[\frac{\hbar\omega}{2k_B T} \right] , \tag{10}$$

where M is the mass of an adatom, and ω is its vibrational frequency. The data were fit with this equation, and the results are the curves shown in Figs. 15(a)–15(e). For the monolayer, D, P_{el}, and $\lambda(k_z)$ were the adjustable parameters. Additionally, the phonon energy was allowed to vary for the multilayers. The values obtained for D and the phonon energy are given in Table V. It is important to note that the values of D are not unique, but depend upon the value of the initial guess given the program. This initial value was determined from the potential that gave the best agreement in the close-coupling calculations. Different starting guesses for D, and also the phonon energy for the multilayers, give equally good fits with different final values for each of the parameters.

The values of $\lambda(k_z)$ are plotted in Figs. 16(a) and 16(b). Again, the actual values are dependent upon the ini-

tial guesses for the multiparameter fits; only the general shape of the curves is the same. For the monolayer, the results are for the two very different beam energies, values for the same k_z represent different incident angles. As mentioned previously, the data at $\Theta_i = 80°$ could be perturbed by scattering off of some bare Ag. However, the Debye–Waller attenuation for scattering from the substrate should be much different, and the value of $\lambda(k_z)$ for the 18 meV beam at about the value of k_z, where $\Theta_i = 70°$, shows reasonable agreement. In fact, the thermal attenuation for He scattering from Ag should be much less than from a Xe monolayer, which would result in $\lambda(k_z)$ being small. It is possible that the Debye–Waller attenuation changes near the angular positions of selective adsorption resonances, but the results for the different overlayers and beam energies all show the same general trend. Only for the bilayer results is there a significant deviation from a fairly smooth monotonic decrease in $\lambda(k_z)$ with increasing k_z.

The same correction was used by Lapujoulade et al.[31] to describe the thermal attenuation of Ne and He scattering

TABLE V. Values of the phonon energy $\hbar\omega$ and well depth D used in the parameterization of the Debye–Waller attenuation for He scattering from Xe overlayers.

Coverage	$\hbar\omega$(meV)	D(meV)
Monolayer	2.8	6.976
Bilayer	1.977	6.973
Trilayer	1.949	6.696
~25 layers	1.616	6.077
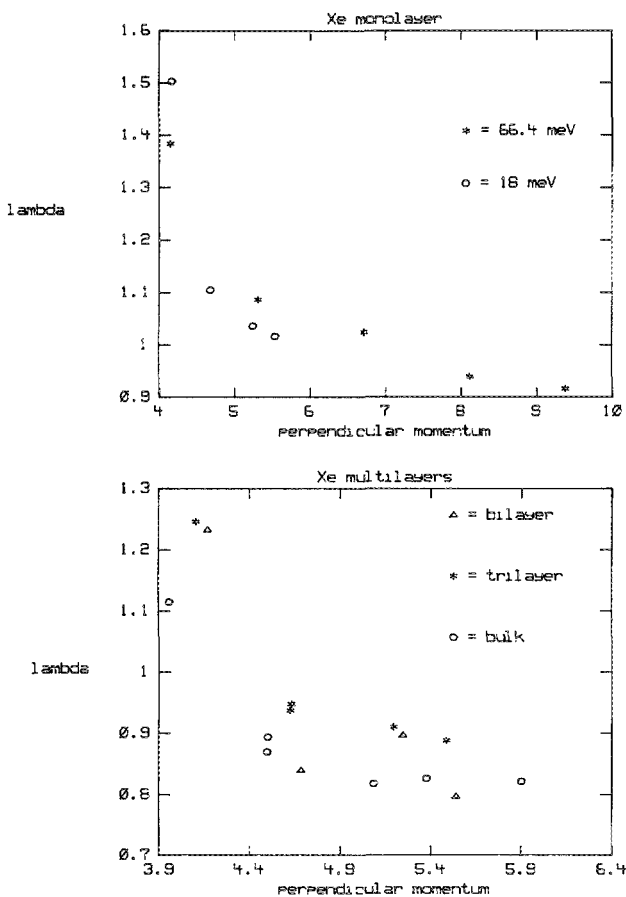
FIG. 16. Plots of $\lambda(k_z)$ $[k_z = k_i(\cos^2\Theta_i + D/E)^{0.5}]$ in the Debye–Waller factors for the Xe overlayers.

from Cu(100). Their derived values of $\lambda(k_z)$ also show an increase for small k_z. One explanation is that the number of surface atoms that the impinging He atoms interact with increases with k_z. The multiple interaction argument requires $\lambda(k_z) < 1$, since the correlated displacement of the multiple surface atoms decreases the Debye–Waller attenuation.[32] However, the parametrization of the Debye–Waller factor that we use is rather crude, and it is difficult to draw any conclusions from the parameters obtained. Since it fits the data reasonably well, it can be used as an empirical correction when comparing the experimental results with the close-coupling calculations.

Fits to the data in Figs. 16(a) and 16(b) were used to obtain values of $\lambda(k_z)$. Thermal attenuation measurements were only made for specular scattering. It was assumed that other diffraction peaks behaved similarly. The only question was how to choose the values of $\lambda(k_z)$ when Θ_i and Θ_f are different. In the following section, the correction

$$I = P_{\text{calc}} \exp\left[-\{\lambda(k_{zi})k_{zi} + \lambda(k_{zf})k_{zf}\}^2 \langle u_z^2 \rangle \right] \quad (11)$$

was used, where k_{zi} and k_{zi} are the perpendicular momenta at Θ_i and Θ_f, respectively, and P_{calc} is the calculated result. For Ar and Kr, not enough data were taken to test this parametrization. For these systems, the results from the two previous papers were used, where $\lambda(k_z)$ was taken as unity for all angles.

THEORY

As mentioned in the Introduction, one of the main purposes of these experiments was to help determine the He–surface interaction potential. In this section, the results of the close-coupling calculations are discussed. Here, we were not interested in constructing an empirical potential to fit the data, but to see if we could reproduce the experimental data using what is experimentally and theoretically known about some terms that might comprise a realistic He–surface potential. Important questions exist about constructing these potentials. As pointed out in Ref. 33, there are at least three important questions. First, what nonadditive three-body or many-body terms have a significant effect on the potential.[7,8,15–17,33–35] It is possible that the total nonadditive correction could be close to zero, as various terms in the complete expansion cancel one another. Next, there is still some question about the position z_0 of the Ag reference plane,[36–38] an important ingredient for computing substrate-mediated effects. Finally, there is the crucial question about the remaining uncertainties in the currently accepted He–RG [RG = Ar, Kr, Xe] pair potentials.[39–41] Since the sum over pair potentials is the most significant part of the total He–surface potential, even fairly small errors in them can obscure the effect of higher order terms. There is also the question about how well purely elastic calculations can reproduce the scattering data when the actual experiments have a high degree of inelastic scattering.

This section is divided into three parts. In the first, we will discuss the terms used to construct the potentials. In the next, the method of solving the coupled equations will be briefly discussed. Finally, the results of the calculations will be presented.

Potentials

The He–surface potentials used were constructed as the sum of four terms,

$$V = V_2 + V_s + V_3^{a-a} + V_3^{s-a} . \quad (12)$$

V_2 is the sum of the He–rare gas pair potentials, $U(r)$, for all of the adatoms, at positions $\mathbf{R}_i$, in each of the layers,

$$V_2(\mathbf{r}) = \sum_i U(\mathbf{r} - \mathbf{R}_i) . \quad (13)$$

V_s is the term for the interaction with the subtrate, including both two-body and multibody contributions. The final two terms are the sums over three-body interactions, either involving a He atom and pairs of adatoms (V_3^{a-a}), or He–adatom–substrate interactions (V_3^{a-s}). The only term considered in Ref. 33 that is not included is a correction to V_2 due to the thermal vibrations of the adatoms. Using the approximation in Ref. 33, this term should be small, $\lesssim 0.1$ meV. For the Ar monolayer, this term would reduce the well depth of the potential by ~ 0.3 meV. This could change the lowest level of the total potential by about 0.1 meV.

V_2

As mentioned in the Introduction, the interaction with an ordered overlayer can be expanded in a Fourier series.

The method for determining $V_{2,\mathbf{G}}(z)$ for the superposition of pair potentials is described in Steele.[42] The result is

$$V_{2,\mathbf{G}}(z) = \frac{2\pi}{a_c} \int_0^\infty J_0(Gt) U[(z^2 + t^2)^{1/2}] t \, dt , \quad (14)$$

where a_c is the area of a unit cell, and J_0 is the zero order Bessel function. The He atoms are sensitive to the large corrugation of the top adlayer, so values of $V_{2,\mathbf{G}}(z)$ for $\mathbf{G} \neq 0$ have to be computed. For the multilayers, $V_{2,0}(z)$ was calculated separately for each layer of adsorbed rare gas, and the results were added to $V_{2,0}(z)$ of the top adlayer.

Three different forms for the pair potentials were used. They were the Hartree–Fock with damped dispersion (HFD),[39–41] the Maitland–Smith (MS),[39,40,43] and the Watanabe–Allnatt–Meath (WAM).[39,44] The HFD potential has the form

$$U(r) = A e^{-\alpha r} - F(r) \sum_{i=0}^{2} \frac{C_{2i+6}}{r^{2i+6}} , \quad (15)$$

where

$$F(r) = \exp\left[-\left(\frac{1.28 r_m}{r} - 1 \right)^2 \right] \quad \text{for } r < 1.28 r_m \quad (16)$$

and

$$F(r) = 1 \quad \text{for } r \geqslant 1.28 r_m . \quad (17)$$

r_m is the position of the minimum of the potential well. The MS potential has the form

$$U(r) = \frac{\epsilon}{n-6} [6x^{-n} - nx^{-6}] , \quad (18)$$

with

$$x = \frac{r}{r_m} \quad \text{and} \quad n = 13 + \gamma(x-1) . \quad (19)$$

ϵ is the well depth. Finally, the WAM potential has the form

$$U(r) = [\gamma(1 + 0.1r) - 1] e^{(a_0 r + a_1 + a_2 r^{-1} + a_3 r^{-2})}$$
$$- F(r) \sum_{i=0}^{2} \frac{C_{2i+6}}{r_{2i+6}} , \quad (20)$$

with

$$F(r) = \exp\left[-0.4 \left(\frac{1.28 r_m}{r} - 1 \right)^2 \right] \quad \text{for } r < 1.28 r_m \quad (21)$$

and

$$F(r) = 1 \quad \text{for } r \geqslant 1.28 r_m . \quad (22)$$

These three different potentials were chosen because of their ability to reproduce crossed-beam gas-phase scattering data and dilute gas bulk properties. For the three He–rare systems studied, the preferred potentials were the HFD fit for He–Ar[39,41] (hereafter referred to as the HFD potential), either the MS or WAM for He–Kr,[39,40] and the MS, or possibly the HFD I, for He–Xe.[39,40] Two slightly different sets of parameters were used for Xe, labeled HFD (I) and HFD (II). The values used for the potential parameters are given in Table VI. Of these potentials, the HFD for Ar is probably the most accurate, and the He–Xe potentials are the least refined.[39]

V_s

The second term is the He–Ag interaction in the absence of any adlayers. Effects of the adsorbate on the total He–Ag potential are considered in the V_3^{a-s} term. Even for a monolayer, the position of the surface adlayer plane is > 3 Å above the top plane of the Ag substrate.[21,22] The distance of closest approach for a He atom is a few Å above the adlayer plane. So, the He atom is always far enough from the Ag substrate that the interaction can be represented by a long range van der Waals attraction,[47,50]

$$V_s(z) = -\frac{C_3}{(z+b)^3} . \quad (23)$$

The value of C_3 is calculated from the polarizability of He and the dielectric response of the substrate.[37] The value used was 249 meV Å³.[51] This value is probably accurate within 10%.[33]

The second parameter in $V_s(z)$ is

$$b = d_\perp - \frac{c}{2} - z_0 , \quad (24)$$

where $d_\perp$ is the distance between the plane of the top adlayer and the plane of the top row of Ag atoms. The second two terms represent the position of the reference plane of the Ag substrate above the plane of the top row of Ag atoms. The values of $d_\perp$ for Xe and Kr come from LEED measurements[21,22]; 3.55 Å for Xe and 3.3 Å for Kr, accurate to within about 0.1 Å. To estimate $d_\perp$ for Ar, the value for physisorption on graphite, 3.2 ± 0.1 Å, was used.[52] For determining the position of the image plane, the geometry in Fig. 1 of Ref. 37 is used. For Ag(111), $c/2$, half of the interplanar spacing of the Ag, is 1.18 Å. The estimate of z_0 is 0.16 Å.[38] Therefore, the estimates of b are 2.2 Å for Xe, 2.0 Å or Kr, and 1.9 Å for Ar. These values are 0.2 Å larger than those used in Ref. 33.

V_3^{a-a}

The third term is the first nonadditive contribution considered. It arises from three-body dispersion forces between the He atoms and pairs of adatoms. V_3^{a-a} is calculated by summing over the Axilrod–Teller–Muto (ATM) triple–dipole interactions[53] for the three atoms involved (A,B,C):

$$E_3(A,B,C) = \nu(A,B,C)$$
$$\times \frac{(1 + \cos \Theta_A \cos \Theta_B \cos \Theta_C)}{(r_{AB} r_{BC} r_{CA})^3} , \quad (25)$$

over all pairs of adatoms. In this equation, the angles are the interior angles of the triangle whose vertices are the three atoms, and r_{AB}, r_{BC}, and r_{CA} are the distances between the atoms. The values of $\nu(A,B,C)$ are calculated from the dynamical polarizabilities of the atoms,[34] the values for a He atom interacting with pairs of adatoms are 6.6 eV Å⁹ for Ar, 13.5 eV Å⁹ for Kr, and 31.5 eV Å⁹ for Xe. These values are probably accurate to within 5%–10%.[34]

To calculate the sums, we used the procedure of Klein *et al.*[35] V_3^{a-a} is periodic in $\mathbf{R}$, and so can be expanded as a Fourier series in the reciprocal lattice vectors $\mathbf{G}$,

TABLE VI. Parameters for the pair-potentials used, and the values for the lattice constants. Monolayer values come from our experiments Ref. 2, and assume an aged monolayer. Values are accurate to ± 0.02 Å. Multilayer lattice constants and interlayer spacing were calculated from data in Ref. 46 using the surface temperatures of the experiments. The lattice constants are within 0.01 Å of the values we measured, Ref. 3, which were accurate to ± 0.02 Å.

	Maitland–Smith	
	Xe(Refs. 39 and 40)	Kr (Refs. 39 and 40)
ϵ(meV)	2.361	2.62
γ	5	4
r_m(Å)	3.98	3.64

	HFD		
	Xe[HFD(I)] (Refs. 40 and 45)	Xe[HFD(II)] (Ref. 39)	Ar[HFD fit] (Refs. 39 and 41)
A(a.u.)	293.5	294.3728	73.72
α(Å^{-1})	3.93	3.926038	3.95293
r_m(Å)	3.93	3.93	3.48
C_6(a.u.)	18.3	18.45	9.82
C_8(a.u.)	336.9	339.57	153.5
C_{10}(a.u.)	7081	7151.3	3248

(N. B. for Xe, the values correspond to the HFDI potentials in the references)

	WAM
	Kr (Refs. 39 and 44)
γ(a.u.)	2.8403
a_0(a.u.)	-2.2100
a_1(a.u.)	5.4070
a_2(a.u.)	-5.8294
a_3(a.u.)	4.5072
r_m(Å)	3.6878
C_6(a.u.)	14.2
C_8(a.u.)	270.1
C_{10}(a.u.)	3760

(N. B. values correspond to XC-2 in Ref. 39 and U_b (D,K) in Ref. 44)

	Lattice constants (Å)		
	Ar	Kr	Xe
Monolayer	3.78	4.02	4.38
Multilayers	3.761	4.00	4.34
Interlayer spacing	3.071	3.265	3.544

$$V_3^{a-a}(z) = V_{3,0}^{a-a}(z) + \sum_{\mathbf{G}_{m,n}\neq 0} V_{3,G}^{a-a}(z)e^{i\mathbf{G}\cdot\mathbf{R}} . \qquad (26)$$

if only the three lowest order G vectors are retained, of length $G_0 = 0$, $G_1 = 4\pi/a\sqrt{3}$, and $G_2 = 4\pi/a$, the sum only needs to be computed for three sites above the lattice. Three representative positions in the unit cell are: on top of an adsorbate atom (A), in the center of the triangle formed by three adatoms (S), and a bridge site between two adatoms (SP). Even in this simple approximation, the laterally averaged value is considerably more than an order of magnitude larger than any of the other terms for the He–surface distances involved. So, only the laterally averaged component is retained,

$$V_3^{a-a}(z) = V_{3,0}^{a-a}(z) = \frac{\Sigma E_{3,A} + 3\Sigma E_{3,SP}}{4} . \qquad (27)$$

The ATM three-body interaction for each pair of adatoms is summed over all of the adatom pairs, with the He atom at lateral positions A and SP a distance z above the surface. The

summations were carried out over a distance of about $8a$ (a is the lattice constant) from the lateral position of the He atom for both sites, and V_3^{a-a} was computed for one, two, three, and eight layers. The sums converge slowly, but this procedure includes enough adatoms to make the results accurate to within 0.1%. Figure 17 shows the results, in reduced form $\Gamma_0(z/a)$, for a monolayer and eight layers. In terms of these functions,

$$V_3^{a-a}(z) = \frac{\nu(\text{A,B,C})}{a^9} \Gamma_0\left(\frac{z}{a}\right) . \qquad (28)$$

For $0.6 \leqslant z/a \leqslant 2.0$, $\Gamma_0(z/a)$ can be fit with a power dependence to better than 2%. For $z/a < 0.6$, an exponential fits the results. The values of these fits are given in Table VII.

As can be seen in Fig. 17, V_3^{a-a} is repulsive. It contributes about 0.3–0.4 meV to the potential at the position of the well minimum. This is a significant contribution to the total potential.
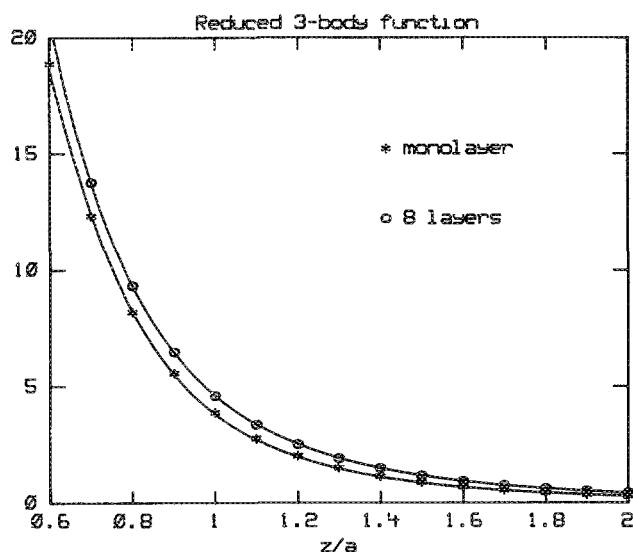
FIG. 17. Plots of the reduced function $\Gamma_0(z/a)$ used to determine V_3^{a-a}. Symbols are calculated points, solid lines used the functions and parameters given in Table VII.

TABLE VII. Values of the fitting parameters for $\Gamma^0(x)$ $(x = z/a)$, the reduced form of V_3^{a-a}. For $x < 0.6$, the fitting function is $A \exp(-Bx^C)$. For $x \geqslant 0.6$, the fitting function is $Ax^{-B}Cx^{-D}$.

Coverage	A	B	C	D
		$z/a < 0.6$		
Monolayer	552.1	8.335	0.7577	
Bilayer	272.4	4.504	0.9564	
Trilayer	249.6	4.180	0.9921	
Eight layers	241.3	4.061	1.007	
		$z/a \geqslant 0.6$		
Monolayer	4.144	3.8	0.323	6.78
Bilayer	8.729	3.972	4.298	4.640
Trilayer	6.003	3.709	1.456	5.059
Eight layers	6.007	3.657	1.389	5.033

V_3^{a-s}

This term takes into account the three-body interaction between a He atom, an adatom, and the substrate. Another method to account for this effect is to increase the value of b in the V_s term.[54] In this paper, V_3^{a-s} is given by the results of Klein et al.,[35] who used the McLachlan theory[55] to derive the equation

$$V_3^{a-s}(z) = -\frac{\pi C_{s2}}{\sqrt{3}a^2(z+2b)^4}.$$ (29)

This result is for a hexagonal close-packed layer. The McLachlan coefficient C_{2s} is given in terms of the frequency dependent polarizabilities of the atoms and the screening response of the substrate. The calculated values for C_{s2} used are 5.09 eV Å^6 for Xe, 3.32 eV Å^6 for Kr, and 2.30 eV Å^6 for Ar.[35,56]

This term contributes about 0.1 meV to the total potential for a monolayer. This is a significant value, but is small enough that its effect can be lost to uncertainties in the other terms of the potential. Since the surface of the multilayers is farther from the Ag substrate, the effect on the potential due to this three-body term will be even weaker, and so it is only included in the total potential for the monolayers.

Scattering calculations

The coupled equations are

$$\frac{\hbar^2}{2m}\left[-\frac{d^2}{dz^2} + (\mathbf{K} + \mathbf{G})^2 - k^2\right]$$

$$\times \psi_G(z) + \sum_{G'} V_{G-G'}(z)\psi_{G'}(z) = 0.$$ (30)

To solve these equations, the total potential was divided into two separate regions. Near the surface, the log derivative method was used.[57] For distances somewhat greater from

the surface than z_m, the variable-interval variable-step integrator of Parker et al.[58] was used.

The code was checked by repeating the calculations of Hutson and Schwartz[15] for the He–Xe/graphite system. This was done using the HFD pair potential and a basis set similar to that of their full basis calculation, and the potential parameters from Smith et al.[40] given in their Table IV, but with $r_m = 7.427$ a.u., which is the correct value from Ref. 40. A comparison of the two calculations shows an agreement of the relative intensities to within about 5%, as well as agreement in the angular positions of all major features. We also compared results using the MS pair potential. The positions of the maxima and minima in the calculated spectra are comparable to those of Hutson and Schwartz, though the differences in the relative intensities are larger than in the case of the HFD pair potential, since we used a much larger basis set than the minimal set used by them.

The scattering calculations were done only for the $\langle 11\bar{2} \rangle$ and $\langle 01\bar{1} \rangle$ azimuths. This allowed the use of symmetrized basis sets, which nearly halves the number of basis functions and greatly reduces the computer time needed. The G vectors which were included depended on the incident angle. The number of channels used varied, but was normally about 60–70. For the 18 meV beam, the criterion was, in general, that $(\hbar^2/2m)(\mathbf{K} + \mathbf{G})^2 \leqslant 75$ meV. Convergence was checked against basis set size, interval size, and step size, and the calculated results presented should be within about 5% of the totally converged value, at least for the results using an 18 meV He beam.

The lowest four bound levels for the laterally averaged part of the He–surface potentials used are shown in Table VIII. These levels were determined with a Numerov–Cooley integrator.[59]

Results

In the figures that follow, the results of the scattering calculations were done at the angles indicated by circles. The dashed lines drawn through the circles are the results of a cubic spline interpolation. They are drawn as a visual aid, but may tend to exaggerate some features in the spectra. The

TABLE VIII. Energies (in meV) of the lowest four bound levels of the He–surface potentials discussed. Also included are the well depth D (meV) and the position of the well minimum z_m (Å).

	E_0	E_1	E_2	E_3	D	z_m
Xe monolayer						
$MS + V_s + V_3^{a-a}$	4.89	2.08	0.73	0.21	7.07	3.54
$MS + V_s + V_3^{a-a} + V_3^{a-s}$	5.00	2.16	0.78	0.23	7.19	3.54
$MS + V_s + V_3^{a-a} + V_3^{a-s}(b = 2.0\ \text{Å})$	5.15	2.26	0.83	0.25	7.37	3.53
$MS + V_s + V_3^{a-a} + V_3^{a-s}(a = 4.40\ \text{Å})$	4.96	2.14	0.77	0.23	7.14	3.54
$MS + V_s + V_3^{a-a} + V_3^{a-s}(a = 4.36\ \text{Å})$	5.04	2.18	0.79	0.23	7.24	3.54
Xe bilayer						
$MS + V_s + V_3^{a-a}$	4.50	1.80	0.56	0.13	6.63	3.56
Xe trilayer						
$MS + V_s + V_3^{a-a}$	4.40	1.72	0.51	0.11	6.52	3.56
Xe bulk						
$MS + V_s + V_3^{a-a}$	4.34	1.66	0.47	0.08	6.45	3.56
$HFD(I) + V_s$	4.31	1.56	0.43	0.08	6.56	3.51
$HFD(II) + V_s$	4.32	1.57	0.43	0.08	6.58	3.52
$HFD(II) + V_s + V_3^{a-a}$	3.90	1.33	0.33	0.05	6.06	3.54
Kr monolayer						
$WAM + V_s + V_3^{a-a}$	5.70	2.41	0.86	0.25	8.22	3.27
$WAM + V_s + V_3^{a-a} + V_3^{a-s}$	5.82	2.50	0.91	0.28	8.35	3.27
$MS + V_s + V_3^{a-a} + V_3^{a-s}$	5.77	2.49	0.91	0.27	8.33	3.23
Kr bilayer						
$WAM + V_s + V_3^{a-a}$	5.08	1.98	0.61	0.15	7.52	3.29
Kr trilayer						
$WAM + V_s + V_3^{a-a}$	4.95	1.87	0.55	0.12	7.37	3.29
Kr bulk						
$WAM + V_s + V_3^{a-a}$	4.86	1.80	0.50	0.09	7.28	3.29
Ar monolayer						
$HFD + V_s + V_{3,C}^{a-a}$	5.80	2.40	0.84	0.25	8.45	3.08
$HFD + V_s + V_3^{a-a} + V_3^{a-s}$	5.92	2.47	0.88	0.26	8.59	3.08
Ar bilayer						
$HFD + V_s + V_3^{a-a}$	4.98	1.83	0.53	0.12	7.52	3.10
Ar trilayer						
$HFD + V_s + V_3^{a-a}$	4.80	1.70	0.45	0.09	7.32	3.10
Ar bulk						
$HFD + V_s + V_{3,C}^{a-a}$	4.73	1.65	0.42	0.07	7.24	3.10
$HFD + V_s + V_3^{a-a}$	4.69	1.61	0.39	0.06	7.20	3.10
$HFD + V_s$	5.00	1.79	0.46	0.08	7.58	3.09

results were corrected for thermal attenuation at the surface temperature of the experiment, using the Debye–Waller factor discussed in the previous section. The calculated selective adsorption results were also multiplied by a factor of

$$\frac{\Delta\Theta_w}{(\Delta\Theta_{\text{inst}}^2 + \Delta\Theta_w^2)^{0.5}} \cdot \qquad (31)$$

In this equation, $\Delta\Theta_{\text{inst}}$ is the FWHM of the instrument function (0.7°) and $\Delta\Theta_w$ is the broadening due to the coherence length of the surface (120 Å). This correction has the effect of further attenuating the results near glancing angles. All of the results labeled as bulk were done using 25 layers.

The experimental results are plotted as solid lines. For the case of the bulk Xe results, a background correction was

estimated from the diffraction spectra, and this was subtracted from the experimental results. Finally, the experimental results for each overlayer have been multiplied by an arbitrary factor to scale the data with the calculations.

There remains a question about how one ought to compare the experimental and theoretical results. It is important to remember that the calculations consider only elastic scattering, and the surfaces studied exhibit a great deal of inelastic scattering. This fact is clearly demonstrated by the Debye–Waller results of the previous section; the surface vibrations decrease the amount of elastic scattering by as much as an order of magnitude. We attempted to at least partially correct for the inelastic scattering by multiplying the theoretical results by Debye–Waller factors determined from the thermal attenuation experiments. As a function of incident angle, these corrections cause a smooth monotonic change in the intensities of the calculations. These corrections are not precise, but should help to make more accurate comparisons between the relative intensities of features in the calculated and experimental spectra. However, the thermal attenuation experiments were only done for a limited number of incident angles. There can be incident angles where there are phonon-assisted processes that would cause the Debye–Waller factor used to be seriously in error. Therefore, there can be regions in the spectra where differences in the relative intensities of various features between the calculated and experimental results are due to inelastic effects, rather than inaccuracies in the He–surface potentials. Also, the calculated points were done for discrete angles and energies, whereas the experimental data points are averaged over

the instrumental resolution of our machine. This can also effect the relative intensities of the spectra.

Although nothing more than qualitative agreement can be expected for the intensities, the overall *shapes* and *angular positions* of the various features in the calculated spectra, relative to those in the experimental data, should be good indicators of the accuracy of the He–surface potentials. The free-atom approximation, Eq. (7), gives qualitative guidance about how the selective adsorption features should move as the bound levels are changed. As the levels become shallower, the selective adsorption features move towards smaller incident angles. This is very clearly shown in Figs. 18(d) and 18(e). The two calculated spectra have similar features, but the features in the one using the potential with the shallower levels systematically occur at more normal angles. In the following discussion, the relative *positions of the features* in the spectra are the primary criteria for determining the accuracy of the He–surface potentials.

Xe overlayers

For a 25 layer film, the substrate–surface distance is ~ 80 Å, and the contribution of the Ag to the total potential will be negligible, < 0.001 meV at r_m. The ability to reproduce the scattering intensities of the thick layers is then a test of the validity of the V_2 and V_3^{a-a} terms in determining the total He–surface potential. If these data cannot be reproduced, then it will be difficult to assess the substrate contribution to the potential in the case of only a few layers. Figures 18(a)–18(c) show the results for scattering from 25
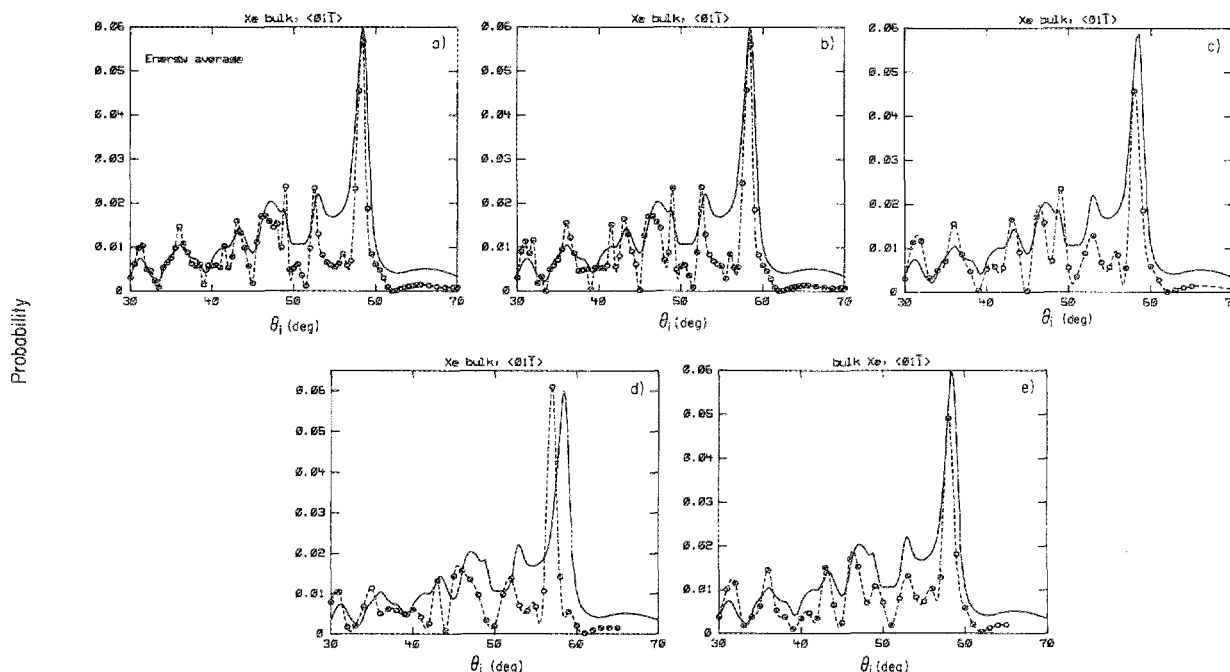
FIG. 18. Comparison between calculated results (circles with dashed lines drawn through them, see the text) and experimental results (solid lines) for specular scattering from 25 layers of Xe along the $\langle 01\bar{1}\rangle$ azimuth. The calculations shown in (a) are an average of calculations at three different energies to take into account the velocity spread of the incident beam (see the text). The total potential was composed of the MS pair potential plus V_s plus V_3^{a-a}. (b) shows the results for only the central energy, 17.9 meV, which is the same energy used for the results plotted in (c)–(e). (c) show the same calculations, but for 1° increments, instead of 0.5° increments. (d) shows the calculations utilizing the HFD(II) pair potential plus V_s plus V_3^{a-a}. (e) shows the calculations utilizing the HFD(II) pair potential plus V_s.

layers of Xe along the less corrugated $\langle 01\bar{1}\rangle$ azimuth, using the MS pair potential and V_3^{a-a}. (For all of the bulk results, V_s was included in the calculations, although the effect is negligible.) The energy averaged results used three different velocities. The Gaussian-shaped incident velocity distribution was divided into three equal area intervals for the range $\pm 3\sigma$ ($\sigma = \text{FWHM}/2.354 = 5.15 \times 10^{-4}$ cm/μs.) Each of these intervals was subdivided into several small regions, and the weighted mean of the velocities was determined,

$$\langle v\rangle = \frac{\Sigma_i w_i v_i}{\Sigma_i w_i}, \tag{32}$$

where w_i is the area of the region with velocity v_i. The resulting velocities were used to determine the energies used in the calculations; 17.686, 17.9, and 18.11 meV. The agreement between the results of Figs. 18(a) and 18(b), which is for the same angular mesh (every 0.5° of polar angle) but for only 17.9 meV He, demonstrate the validity of using only the peak velocity of the distribution for the calculations, at least for a narrow velocity distribution, such as that used here.

The results of the scattering calculations do a very good job of reproducing the data, as can be seen in Fig. 18(a). Here, we should note the good agreement in the angular positions of the peaks located at ~58°, 36°, and 31°, and the minimum at 45°, or, more generally, the regions between 30°–49° and 45°–50°. The results shown in Fig. 18(b), as mentioned above, are for the same mesh size as those shown in Fig. 18(a), but for the most probable energy, and are nearly identical with the energy averaged results. Figure 18(c) shows the effect of a larger mesh size (1°) on the appearance of the calculated spectrum. Apparent shifts in some features, on the order of ~0.5°, can be seen. Also, a coarser mesh size can occasionally change the qualitative appearance of the spectrum at some angles, due to the absence of sharp features, as can be seen at ~41.5° in Fig. 18(c) vs 18(b). Figures 18(c)–18(e) show comparisons for different potentials, using the same mesh size and beam energy. The difference between the results shown in Figs. 18(c) and 18(d) is the choice of pair potential, V_3^{a-a} being included in each. It can be seen that using the HFD(II) pair potential, Fig. 18(d), leads to a much poorer agreement with experiment as compared with the MS pair potential, Fig. 18(c). In particular, the features at 58°, 45°, 36°, and 31° are all shifted towards more normal angles when the HFD(II) pair potential is used, indicating that the bound levels of the He–surface potential are too shallow. Finally, Fig. 18(e) shows the effect of removing V_3^{a-a}, the ATM triple–dipole contribution. We see immediately that the calculation is very sensitive to the presence of this term, i.e., shifts occur in the calculated spectra which are larger than the instrumental resolution. The removal of V_3^{a-a} improves the agreement between experiment and theory when the HFD(II) pair potential is used. Furthermore, the calculated spectra shown in Figs. 18(c) and 18(e) are in good agreement. Table VIII shows that the bound levels for these two potentials are nearly identical.

Some comment on the information that can be extracted from Figs. 18(c)–18(e) is now in order. It is known that the MS and HFD(II) He–Xe pair potentials both reasonably

reproduce the gas-phase data. Furthermore, we have shown above that when the same higher order terms are used in surface scattering calculations with these two pair potentials, considerable differences occur, e.g., Figs. 18(c) and 18(d). This demonstrates the *extreme sensitivity* that surface scattering has to the potential, but presents us with a dilemma. If the results shown in Figs. 18(c) and 18(d) had agreed with each other, we would have been able to conclude that the two forms of the pair potential were nearly equivalent, allowing us to test whether the ATM triple–dipole term is in fact a good representation of the overall multibody contribution to the He–Xe surface potential (i.e., whether there are other multibody terms that significantly contribute to the total He–surface potential). However, since the calculations shown in Figs. 18(c) and 18(d) do not agree, we cannot carry out this assessment.

If the ATM triple–dipole term is the dominant multibody contribution to the He–Xe(111) surface potential, then our results show that the MS potential is a better representation of the He–Xe pair potential than is the HFD(II) potential. This is consistent with the conclusions of Aziz.[39]

Table IX shows the calculated diffraction probabilities. There is somewhat better agreement with experiment using the MS pair potential plus V_3^{a-a}, but there is not enough data to make a firm conclusion. It should also be remembered that the Debye–Waller correction for diffraction peaks is only tentative, as it is based on specular data, which may tend to skew the corrected results.

Figures 19(a)–19(d) show calculations for scattering along the $\langle 11\bar{2}\rangle$ azimuth. Figure 19(a) is the results using the MS pair potential plus V_3^{a-a}. The potential does not reproduce the experimental data in this direction as well as along the $\langle 01\bar{1}\rangle$ azimuth. The general features are reasonable, but the calculated feature at $\Theta \approx 62°$ has much more intensity and appears shifted with respect to the experimental data. The mesh for the calculations was 0.2° for small angles, so the sharp feature in the calculation at $\Theta \approx 35°$ may be obscured in the experimental data by the instrument resolution. However, the peak in the calculation at $\Theta \approx 41°$ is broad enough that there should be some hint of it in the experimental data, but there is not. Figure 19(b) is the same calculation for a 1° mesh, for comparison with the rest of the calculations. Figure 19(c) shows the results when the HFD(II) pair potential plus V_3^{a-a} is used. The agreement of the calculations with the experimental data is substantially worse, with an overall shift of the features in the calculations towards smaller angles. This is the same trend that was seen for the $\langle 01\bar{1}\rangle$ azimuth, which again indicates that the bound levels of the potential are too shallow. However, when just the HFD(I) pair potential is used, Fig. 19(d), the agreement is about as good as for the MS plus V_3^{a-a}, Figure 19(b). This result is in agreement with what was seen for the $\langle 01\bar{1}\rangle$ azimuth. Table IX shows the calculated diffraction probabilities for the two preferred potentials. They both have about the same ability to crudely predict the experimental results.

Figures 20 and 21 show the results of the calculations for the trilayer and bilayer. The potential in both cases was composed of the MS pair potential plus V_3^{a-a} plus V_s. The agree-

TABLE IX. Calculated diffraction probabilities for ~ 18 meV He scattering from Xe monolayer and bulk. The energies of the calculations are the same as those used in the selective adsorption calculations, and so are slightly different than the experimental energies of the diffraction experiments. The results using the MS pair potential plus V_s plus V_3^{a-a} for 25 layers along the $\langle 01\bar{1}\rangle$ azimuth are the energy-averaged values. The numbers in parentheses are the probabilities after Debye–Waller correction to the experimental surface temperatures.

Θ_i (deg)	Diffraction rod	$MS + V_s + V_3^{a-a} + V_3^{a-s}$	$MS + V_s + V_3^{a-a}$
		Monolayer, $\langle 11\bar{2}\rangle$	
45	$(1\bar{1})$	$5.0\times10^{-2}(7.2\times10^{-3})$	$5.9\times10^{-2}(8.4\times10^{-3})$
	(00)	$1.2\times10^{-1}(3.8\times10^{-2})$	$1.3\times10^{-1}(4.2\times10^{-2})$
	$(\bar{1}1)$	$5.0\times10^{-3}(1.4\times10^{-3})$	$8.0\times10^{-3}(2.2\times10^{-3})$
	$(\bar{2}2)$	$4.5\times10^{-2}(1.2\times10^{-2})$	$4.1\times10^{-2}(1.1\times10^{-2})$
50	(00)	$1.8\times10^{-1}(5.6\times10^{-2})$	$1.7\times10^{-1}(5.5\times10^{-2})$
	$(\bar{1}1)$	$2.0\times10^{-2}(5.3\times10^{-3})$	$1.5\times10^{-2}(4.0\times10^{-3})$
	$(\bar{2}2)$	$1.6\times10^{-2}(3.9\times10^{-3})$	$1.8\times10^{-2}(4.2\times10^{-3})$
70	(00)	$\cdots$	$1.8\times10^{-1}(4.2\times10^{-2})$
	$(\bar{1}1)$	$\cdots$	$1.0\times10^{-1}(2.6\times10^{-2})$
	$(\bar{2}2)$	$\cdots$	$1.5\times10^{-2}(3.3\times10^{-3})$
	$(\bar{3}3)$	$\cdots$	$5.0\times10^{-4}(1.0\times10^{-4})$

Θ_i (deg)	Diffraction rod	$MS + V_s + V_3^{a-a}$	$HFD + V_s$
		25 layers, $\langle 11\bar{2}\rangle$	
30	$(1\bar{1})$	$1.6\times10^{-2}(1.8\times10^{-3})$	$1.5\times10^{-2}(1.6\times10^{-3})$
	(00)	$4.7\times10^{-2}(3.4\times10^{-3})$	$2.8\times10^{-2}(2.0\times10^{-3})$
40	$(1\bar{1})$	$1.9\times10^{-1}(2.4\times10^{-2})$	$1.8\times10^{-1}(2.3\times10^{-2})$
	(00)	$1.6\times10^{-1}(1.6\times10^{-2})$	$1.3\times10^{-1}(1.4\times10^{-2})$
	$(\bar{1}1)$	$1.4\times10^{-2}(1.1\times10^{-3})$	$1.1\times10^{-2}(8.5\times10^{-4})$
45	$(1\bar{1})$	$5.7\times10^{-2}(1.3\times10^{-3})$	$4.8\times10^{-2}(1.1\times10^{-3})$
	(00)	$7.4\times10^{-2}(9.5\times10^{-3})$	$6.3\times10^{-2}(8.1\times10^{-3})$
	$(\bar{1}1)$	$9.0\times10^{-4}(8.1\times10^{-5})$	$2.5\times10^{-3}(2.2\times10^{-4})$
	$(\bar{2}2)$	$4.3\times10^{-2}(3.3\times10^{-3})$	$3.5\times10^{-2}(2.6\times10^{-3})$
50	(00)	$3.9\times10^{-2}(5.9\times10^{-3})$	$2.3\times10^{-2}(3.5\times10^{-3})$
	$(\bar{1}1)$	$2.7\times10^{-2}(2.8\times10^{-3})$	$2.4\times10^{-2}(2.5\times10^{-3})$
	$(\bar{2}2)$	$7.5\times10^{-2}(6.4\times10^{-3})$	$6.5\times10^{-2}(5.5\times10^{-3})$
	$(\bar{3}3)$	$6.4\times10^{-2}(5.3\times10^{-3})$	$5.4\times10^{-2}(4.5\times10^{-3})$
60	(00)	$1.7\times10^{-2}(3.3\times10^{-3})$	$4.1\times10^{-2}(7.7\times10^{-3})$
	$(\bar{1}1)$	$7.9\times10^{-2}(1.0\times10^{-2})$	$8.1\times10^{-2}(1.1\times10^{-2})$
	$(\bar{2}2)$	$1.1\times10^{-1}(1.1\times10^{-2})$	$1.1\times10^{-1}(1.1\times10^{-2})$
	$(\bar{3}3)$	$5.2\times10^{-2}(4.9\times10^{-3})$	$5.7\times10^{-2}(5.3\times10^{-3})$
70	(00)	$2.3\times10^{-1}(2.9\times10^{-2})$	$\cdots$
	$(\bar{1}1)$	$1.8\times10^{-1}(2.1\times10^{-2})$	$\cdots$
	$(\bar{2}2)$	$1.0\times10^{-1}(8.7\times10^{-3})$	$\cdots$
	$(\bar{3}3)$	$3.4\times10^{-2}(2.6\times10^{-3})$	$\cdots$

Θ_i (deg)	Diffraction rod	$MS + V_s + V_3^{a-a}$	$HFD + V_s$
		25 layers, $\langle 01\bar{1}\rangle$	
40	(00)	$6.6\times10^{-2}(7.0\times10^{-3})$	$4.0\times10^{-2}(4.2\times10^{-3})$
	$(\bar{2}1)$	$4.8\times10^{-3}(3.3\times10^{-4})$	$1.8\times10^{-2}(1.2\times10^{-3})$
50	(00)	$4.4\times10^{-2}(6.8\times10^{-3})$	$6.1\times10^{-2}(9.4\times10^{-3})$
	$(\bar{2}1)$	$1.4\times10^{-3}(1.3\times10^{-4})$	$1.2\times10^{-4}(1.0\times10^{-5})$
60	(00)	$4.9\times10^{-2}(9.4\times10^{-3})$	$4.7\times10^{-2}(9.0\times10^{-3})$
	$(\bar{2}1)$	$7.7\times10^{-3}(8.2\times10^{-4})$	$9.0\times10^{-3}(9.7\times10^{-4})$
70	(00)	$1.4\times10^{-2}(1.7\times10^{-3})$	$\cdots$
	$(\bar{2}1)$	$3.9\times10^{-3}(3.5\times10^{-4})$	$\cdots$

ment with experiment is about as good as was the case for Xe bulk in the $\langle 11\bar{2}\rangle$ direction. The feature at $\Theta \approx 62°$ is still too large and appears somewhat shifted with respect to the experimental data. However, the experimental data now show a small peak at $\Theta \approx 41°$, where the calculation predicts an increase in the scattering intensity. Table VIII shows how the levels get slightly deeper as the surface–substrate distance decreases.

Figures 22(a)–22(d) show the results for scattering from a Xe monolayer along the $\langle 01\bar{1}\rangle$ azimuth. Figures 22(a) and 22(b) are for the MS pair potential plus V_3^{a-a} plus V_s plus V_3^{a-s}. Figure 22(a) shows an average for the energies 18, 18.18, and 18.36 meV, while Fig. 22(b) is the calculation for just the central energy, 18.18 meV. The calculated results shown in these two figures are virtually identical. Figure 22(c) shows the results when the small attractive term V_3^{a-s}
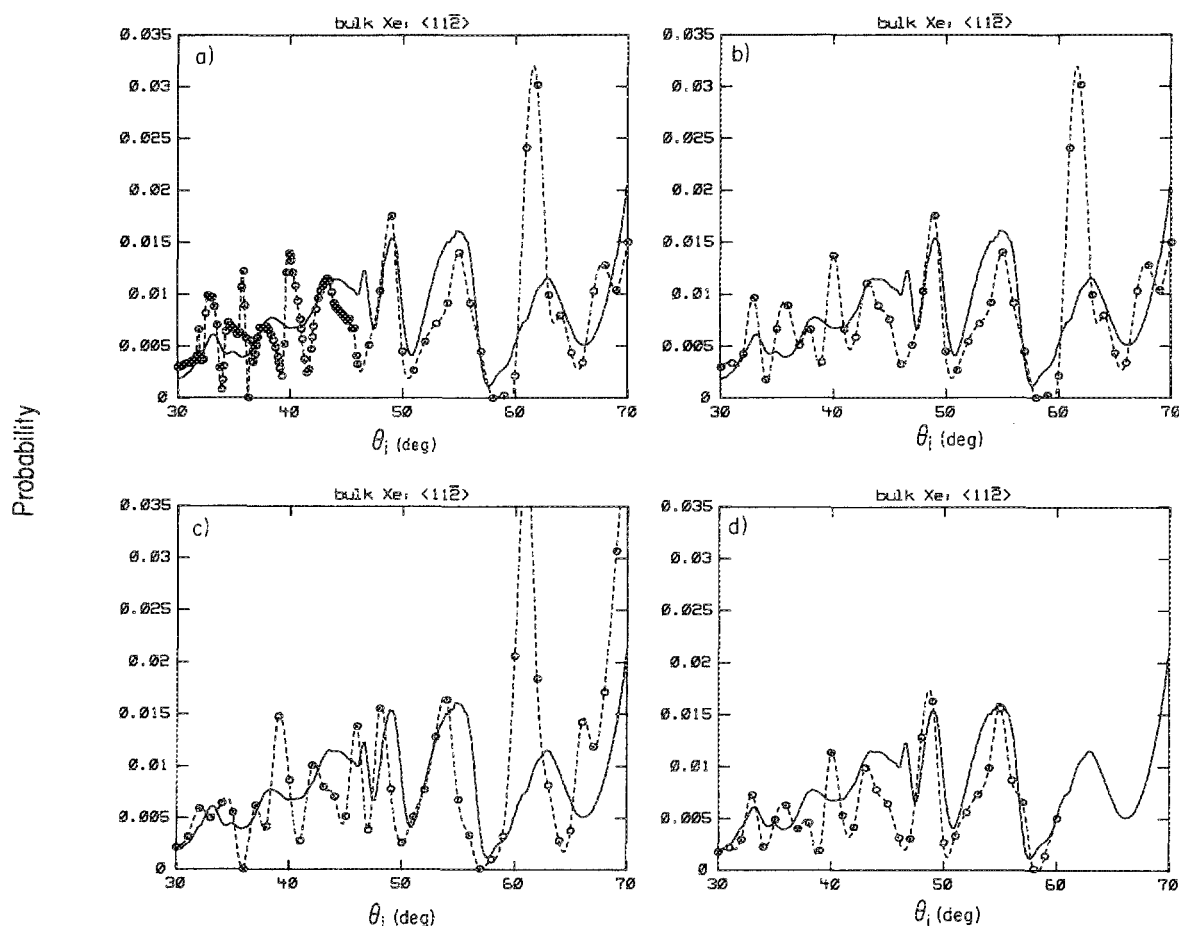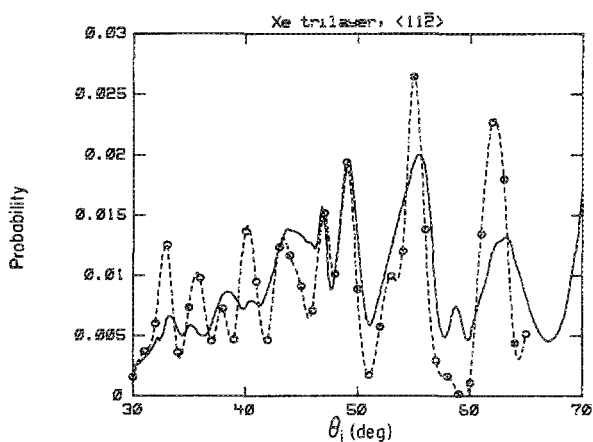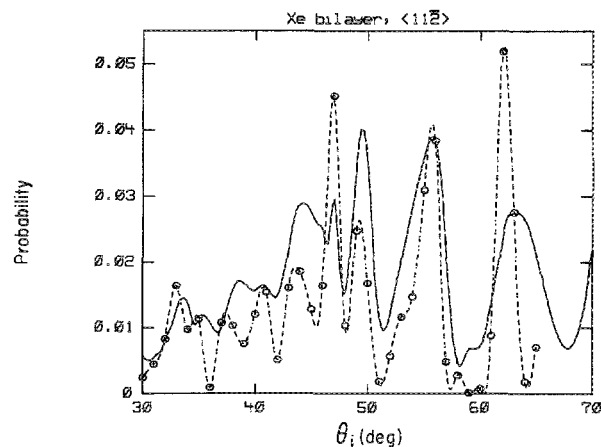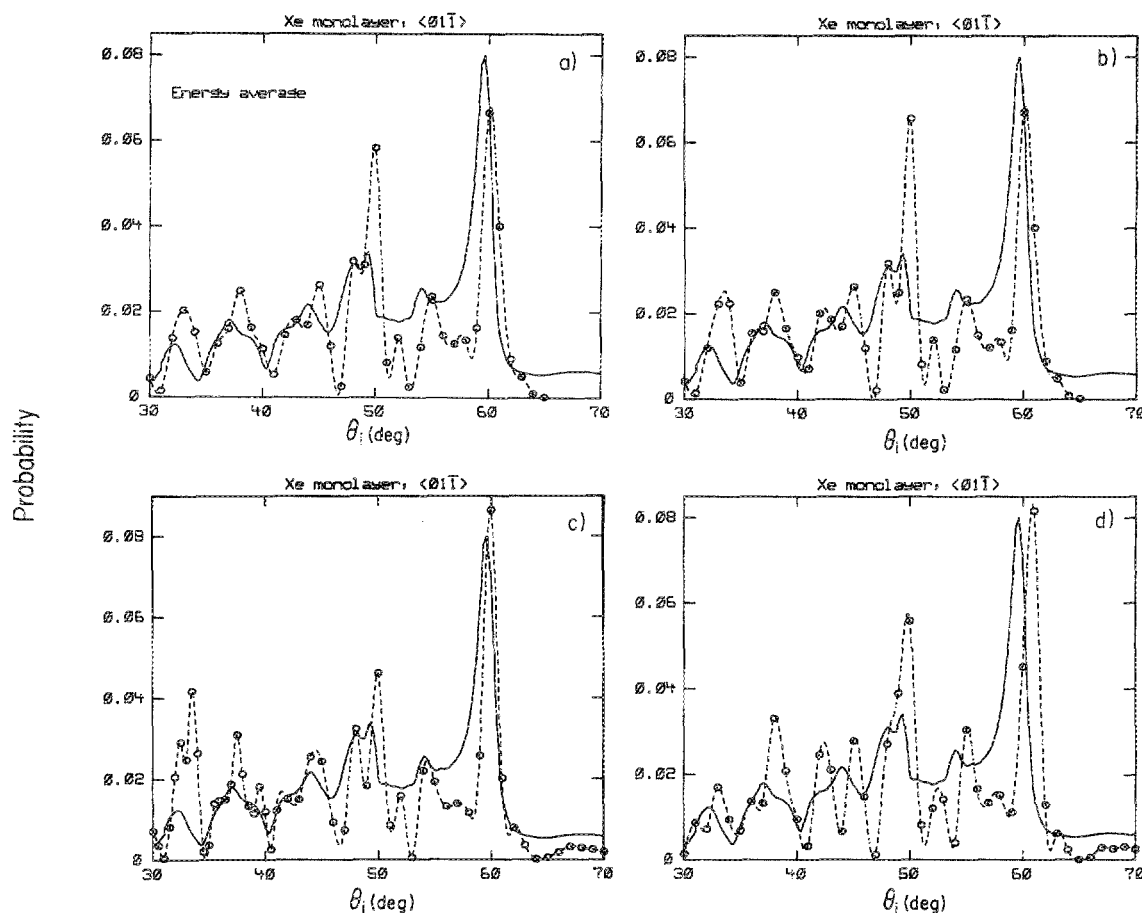
FIG. 19. Comparison between calculated and experimental results for scattering from 25 layers of Xe along the $\langle 11\bar{2} \rangle$ azimuth $E = 17.856$ meV. (a) and (b) show calculations which used the MS pair potential plus V_s plus V_3^{a-a}, with different angular increments for the calculations. The results shown in (c) used the HFD(II) pair potential plus V_s plus V_3^{a-a}. The results shown in (d) used the HFD(I) pair potential plus V_s.

is not included. Though neither potential does a perfect job of reproducing the experimental data, the slightly shallower potential of Fig. 22(c), which neglects the V_3^{a-s} term, lines up better at glancing angles (54° and 60°), where small differences in the bound state energies should be most apparent. The levels predicted by both of these potentials are within

the experimental error of the values determined by the method described in the experimental results section. Figure 22(d) shows the results when the value of b in the V_s term is reduced to 2 Å. The calculated spectrum shifts towards more glancing angles, apparent at 54° and 60°, indicating that this value of b makes the bound levels of the potential too deep.

FIG. 20. Comparison between calculated and experimental results for scattering from a Xe trilayer along the $\langle 11\bar{2} \rangle$ azimuth $E = 17.978$ meV. The calculated results used the MS pair potential plus V_s plus V_3^{a-a}.

FIG. 21. Comparison between calculated and experimental results for scattering from a Xe bilayer along the $\langle 11\bar{2} \rangle$ azimuth $E = 17.968$ meV. The calculated results used the MS pair potential plus V_s plus V_3^{a-a}.

FIG. 22. Comparison between calculated and experimental results for scattering from a Xe monolayer along the $\langle 01\bar{1}\rangle$ azimuth. The calculations shown in (a) are an average of calculations at three different energies to take into account the velocity spread of the incident beam (see the text). The total potential was composed of the MS pair potential plus V_s plus V_3^{q-a} plus V_3^{q-s}. (b) shows the results for only the central energy, 18.18 meV, which is the same energy used for the results plotted in (c) and (d). (c) shows the results of calculations using the MS pair potential plus V_s plus V_3^{q-a}. (d) shows the results of calculations which used the MS potential plus V_s plus V_3^{q-a} plus V_3^{q-s}, but with $b \approx 2.0$ Å.

Finally, there are the results for scattering from monolayer Xe along the $\langle 11\bar{2}\rangle$ azimuth. The calculations shown used the MS pair potential V_3^{q-a} plus V_s with V_3^{q-s} [Fig. 23(a)] and without V_3^{q-s} [Fig. 23(b)]. There is a peak in the calculations at $\Theta \approx 42°$ that does not show up in the experimental data, and the intensity at $\Theta \approx 55°$ is seriously off. For this azimuthal direction, the comparison between the calculated and experimental results does not demonstrate a clear preference for one of the potentials. However, the potential without V_3^{q-s} may be the best choice. The peak positions between 45° and 55° appear to be slightly closer to the experimental results than for the potential that includes the V_3^{q-s} term. Also, the peak at $\Theta \approx 64°$ is more closely reproduced by the potential without V_3^{q-s}. The diffraction probabilities given in Table IX show that the two potentials are about equivalent in their ability to qualitatively reproduce the experimental data.

The reproducibility of all the Xe multilayer spectra was excellent. This is typified by the agreement the bulk Xe results shown in Figs. 9(d) and 19, which were taken several months apart. The reproducibility of the selective adsorption spectra for the monolayer was not as good. This can be seen in Figs. 23 and 24, which also show spectra taken sever-

al months apart. The measured beam energy for the experiment shown in Fig. 24 was 17.97 meV, only slightly higher than for the spectrum shown in Fig. 23, so a comparison with the same calculations is reasonably valid. For the data in Fig. 24, the agreement between theory and experiment is better for $\Theta > 40°$, at least in the peak positions. The reason for the slight disparity between the two experiments is unknown. That the spectra are nearly reproducible means that comparisons with theory are valid, but details may be lost to variability in the monolayers.

One source of uncertainty is the error in the lattice constants. This is particularly the case for the Xe monolayer, which contracts over time. As mentioned, the selective adsorption experiments were done on surfaces that were aged long enough to keep the amount of shrinkage to a minimum. Even so, the experimental measurements are only good to ± 0.02 Å. Table VI lists the lattice constants used. However, to get an idea of the effect of this uncertainty, we did calculations which used all of the potential terms considered for a Xe monolayer, with lattice constants of 4.36, 4.38, and 4.40 Å. The results are shown in Figs. 25(a)–25(c). The mesh size is somewhat course for a detailed comparison, but the overall shapes of the spectra are qualitatively similar.
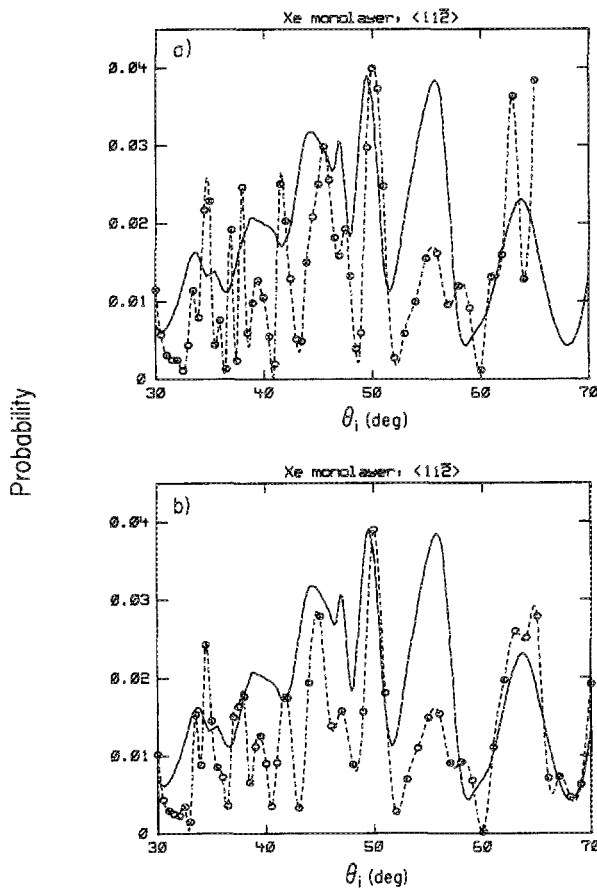
FIG. 23. Comparison between calculated and experimental results for scattering from a Xe monolayer along the $\langle 11\bar{2}\rangle$ azimuth $E = 17.928$ meV. The results shown in (a) used the MS pair potential plus V_s plus V_3^{a-a} plus V_3^{a-s}. The result plotted in (b) used the MS pair potential plus V_s plus V_3^{a-a}.
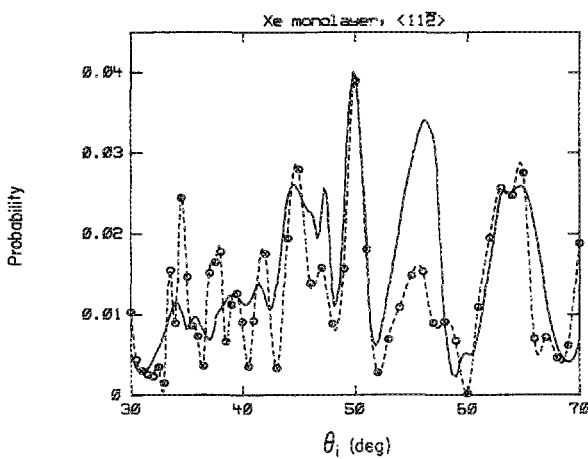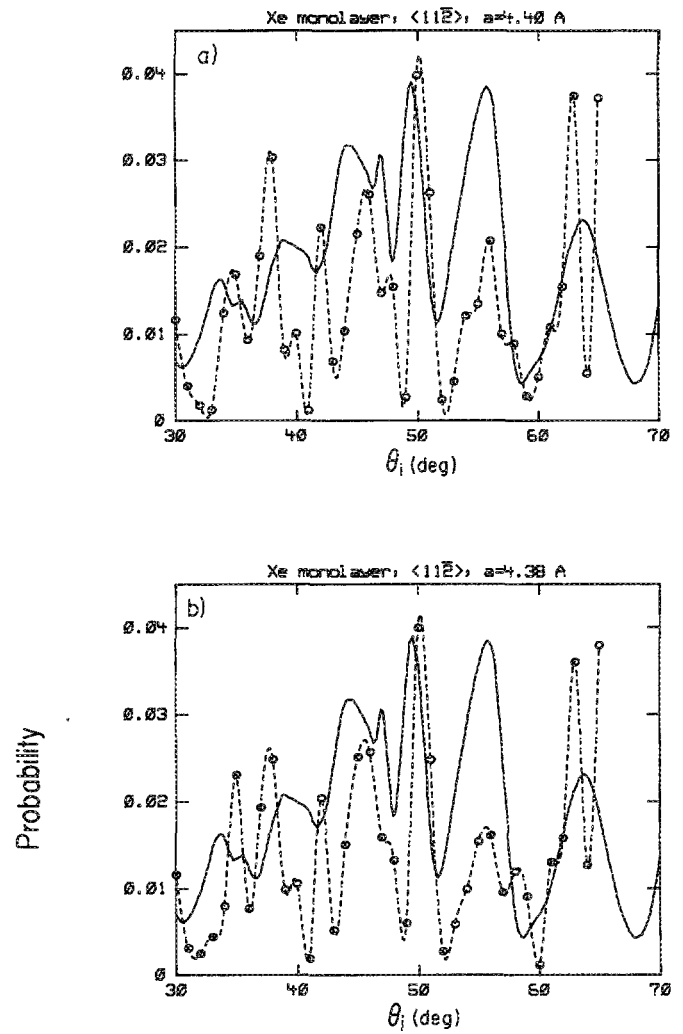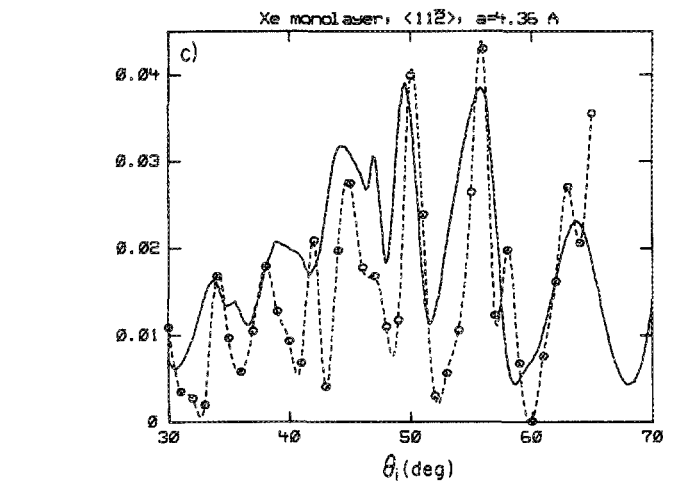

FIG. 24. Comparison between calculated and experimental results for scattering from a Xe monolayer along the $\langle 11\bar{2}\rangle$ azimuth $E = 17.928$ meV. The potential used was the MS pair potential plus V_s plus V_3^{a-a}. The experimental results are for a different monolayer than previously shown, and the experimental beam energy was 17.97 meV, $T_s = 24$ K.

FIG. 25. Comparison between calculated and experimental results for scattering from a Xe monolayer along the $\langle 11\bar{2}\rangle$ azimuth $E = 17.928$ meV. The potential used was the MS pair potential plus V_s plus V_3^{a-a} plus V_3^{a-s}. As indicated, the calculations used three different lattice constants.

This may not be particularly surprising, as the bound levels in the potential do not change by much, as shown in Table VIII. What is apparent is that, at least for certain regions in the calculated spectra, the intensities can change markedly. This makes it more difficult to make judgements about potential choices when comparing the relative intensities of the calculations with the experimental data. It is also interesting to note that all three calculations have a peak at $\Theta \approx 42°$, and the peak at $\Theta \approx 65°$ is a doublet. If the difference between the two different monolayers were due to a change in the lattice constant within this range, the features should appear in both experimental spectra.

In Figs. 26(a) and 26(b), the results of the calculations using the MS pair potential plus V_3^{a-a} are plotted for the two symmetry directions. The vertical lines represent the positions of zeroth order resonances, using the lowest three bound levels of the laterally averaged potential, and the same G vectors as in Figs. 9(a) and 10(a). The point here is that these positions *do not* always fall upon a maximum or mini-mum in the spectra. At least along these symmetry directions, the free-atom approximation is often a relatively poor predictor of the band structure.

Finally, a calculation was done to compare with the experimental data taken with a room temperature beam, using the MS pair potential plus V_3^{a-a} plus V_s. The results are shown in Fig. 27. The calculations may not be as fully converged as the 18 meV results. Uncertainty in the incident beam velocity would obscure small details in the total potential, but the agreement between theory and experiment is surprisingly good. Again, there seems to be structure near glancing angles that the experiment does not pick up. The results also show why a low energy beam is preferred, as the Debye–Waller attenuation obscures many of the features, particularly near normal incidence.

Kr overlayers

For bulk Kr, we used the WAM pair potential plus V_3^{a-a}. The results are shown in Figs. 28(a) and 28(b), with two different mesh sizes for the calculation. The overall fit is worse than for bulk Xe in the $\langle 11\bar{2}\rangle$ direction. There is con-siderable disagreement near $\Theta \approx 54°$, where the calculations show a doublet which should be resolvable with our machine, and yet which is not reflected in the experimental data. Also, as was the case for Xe, there is considerable dis-agreement in the intensity for the peak above 60°. It is also interesting to note that the calculation shows a rather large peak at $\Theta \approx 38°$ where there is only a very small peak in the experimental spectrum. The large increase in intensity at $\Theta \approx 44°$ is probably a threshold. Between 43° and 44°, $G_{1,1}$, which had considerable intensity when open, becomes a closed channel. This is not reflected in the data, though the dispersion of the incident beam velocity distribution may somewhat smooth it out. Good agreement in the positions of the experimental and theoretical features is found in the re-gion between 40° and 50°.

Figures 29 and 30 show the results for the trilayer and bilayer, with the quality of these fits being similar to that of the bulk. Finally, Figs. 31(a)–31(d) show the monolayer
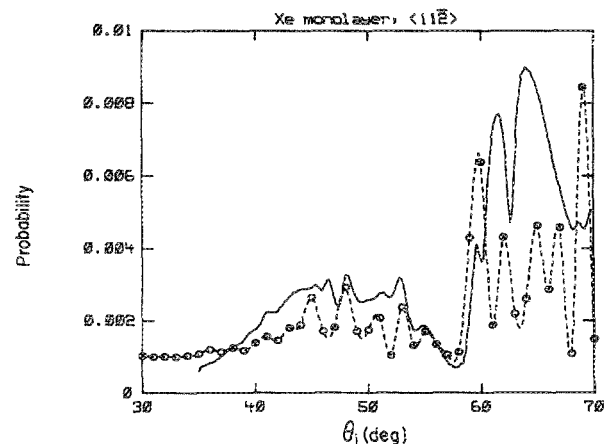

FIG. 26. Calculations for scattering from a Xe monolayer along the two symmetry directions. The potential used was the MS pair potential plus V_s plus V_3^{a-a}. The vertical lines indicate the positions of resonances in the free-atom approximation, using the lowest three calculated values for the levels of V_0 and the coupling G vectors shown in Fig. 13. For the $\langle 11\bar{2}\rangle$ azimuth, there are, from left to right, 0–22, 2–20, 1–20, 0–20, 2–11, 1–11, 0–11, the overlapping 2–01 and 2–10, and the overlapping 1–01 and 1–10. For the $\langle 01\bar{1}\rangle$ azimuth, these are, from left to right, the overlapping 1–22 and 1–20, the overlapping 0–22 and 0–20, the overlapping 2–11 and 2–10, the overlap-ping 1–11 and 1–10, and the overlapping 0–11 and 0–10. This figure is anal-ogous to the plots of the experimental data shown in Figs. 9(a) and 10(a).

FIG. 27. Comparison between calculated and experimental results for scat-tering from a Xe monolayer along the $\langle 11\bar{2}\rangle$ azimuth $E = 66.88$ meV. The potential used was the MS pair potential plus V_s plus V_3^{a-a}.
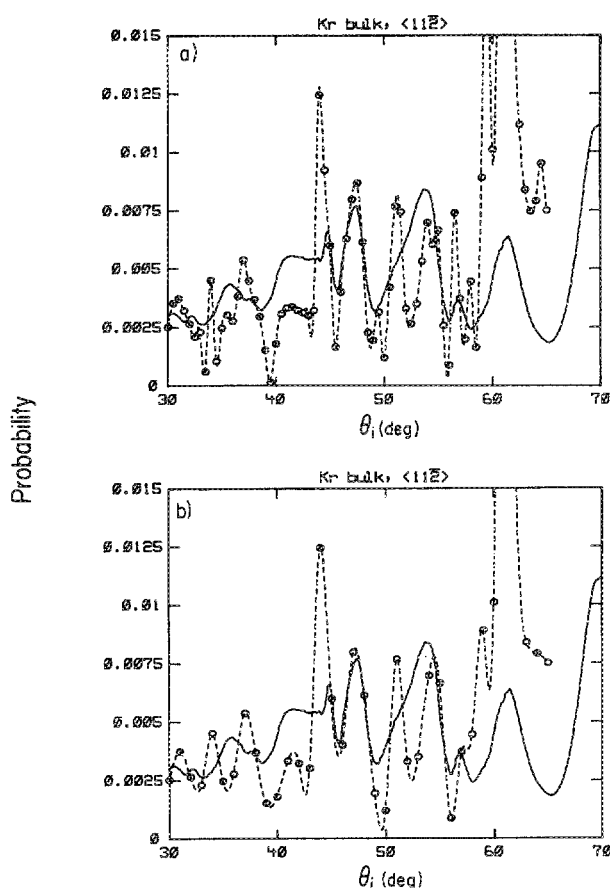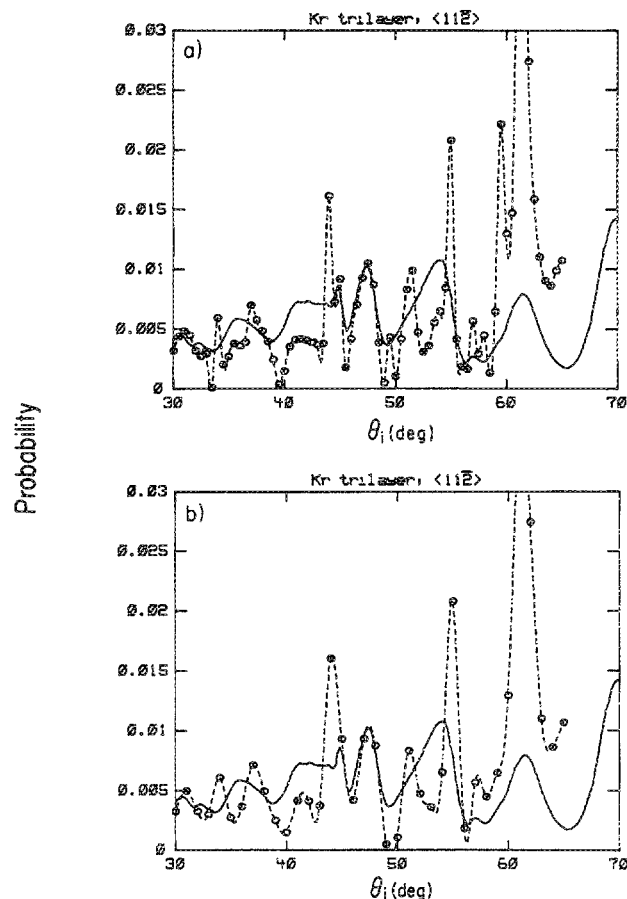
FIG. 28. Comparison between calculated and experimental results for scattering from 25 layers of Kr along the $\langle 11\bar{2} \rangle$ azimuth $E = 18.11$ meV. The potential used was the WAM pair potential plus V_s plus V_3^{a-a}. The difference between the results shown in (a) and (b) is the angular increment of the calculations.

FIG. 29. Comparison between calculated and experimental results for scattering from a Kr trilayer along the $\langle 11\bar{2} \rangle$ azimuth $E = 18.05$ meV. The potential used was the WAM pair potential plus V_s plus V_3^{a-a}. The difference between the results shown in (a) and (b) is the angular increment of the calculations.

calculations. Figures 31(a) and 31(b) are for the WAM pair potential plus V_3^{a-a} plus V_s, with two different mesh sizes for the calculations. The calculation in Fig. 31(c) included the V_3^{a-s} term. Both potentials give similar results, and the agreement is worse than was the case for the multilayers. Even the features that the calculations somewhat reproduce seem to be shifted to somewhat more glancing incident angles. This is an indication that the bound levels of the total potential are too deep. Finally, the calculation shown in Fig. 31(d) uses the same terms in the total potential as the results shown in Fig. 31(c), except that the MS pair potential was used. The calculations shown in these two figures are almost in total agreement, and the bound levels are nearly identical, as shown in Table VIII. This indicates that, within our experimental resolution, we cannot differentiate between these two pair potentials.

Ar overlayers

Figures 32(a)–32(d) show the comparison between the calculations and the experiment for Ar bulk along the $\langle 11\bar{2} \rangle$ azimuth. Before proceeding, it should be noted that some of the calculations used a different parametrization for $\Gamma^0(z/a)$.[33]

$$\Gamma_0\left(\frac{z}{a}\right) = 214 \exp\left(\frac{-4.065z}{a}\right). \tag{33}$$

This is essentially the same as $\Gamma^0(z/a)$ for the monolayer, using the fit given in Table VIII. As shown in Table VIII, there is a small difference in V_0, depending upon which function is used for V_3^{a-a}. For the rest of this discussion, the different three-body term will be referred to as $V_{3,C}^{a-a}$. Figure 32(a) is an average for three different energies over the velocity distribution of the beam. As was the case for Xe, the incident velocity distribution was divided into three equal area regions over the interval $\pm 3\sigma (\sigma = 5.68 \times 10^{-4}$ cm/μs), but just the average velocity for each region was used. The resulting three energies were 17.652, 18.028, and 18.402 meV. Figure 32(b) shows the calculation for 18.028 meV. The potential used was the HFD pair potential plus V_s plus $V_{3,C}^{a-a}$. Figure 32(c) shows the same calculation, but using V_3^{a-a} instead. The difference in these two calculations is negligible. The overall match between theory and experiment is good, with especially good agreement occurring between about 42° and 47°. As mentioned previously, the peak in the experimental data at $\Theta \approx 55°$ could be due to some misaligned Ar islands. A calculation for scattering along the $\langle 01\bar{1} \rangle$ azimuth appears similar to the result for Xe, Fig. 18,
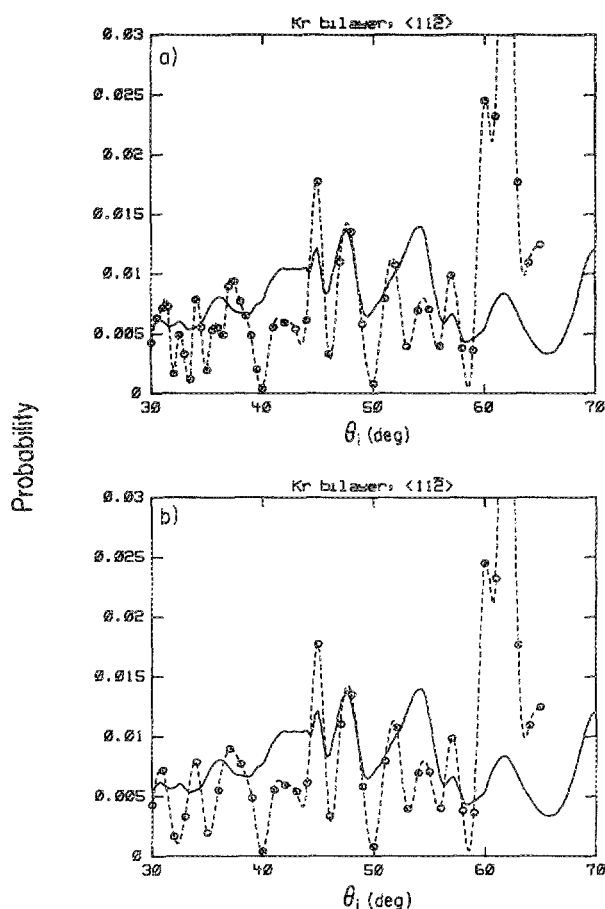
FIG. 30. Comparison between calculated and experimental results for scattering from a Kr bilayer along the $\langle 11\bar{2}\rangle$ azimuth $E = 18.05$ meV. The potential used was the WAM pair potential plus V_s plus V_3^{a-a}. The difference between the results shown in (a) and (b) is the angular increment of the calculations.

with the large peak occuring at this angle.

Before claiming that this total potential well represents the data, a comparison must be done with the calculations shown in Fig. 32(d), which is for the same pair potential without the V_3^{a-a} term. As shown in Table VIII, the difference in V_0 is not inconsequential, and yet, at least for the mesh size of these calculations, the ability of the two potentials to reproduce the experimental data is not much different. The potential which includes the V_3^{a-a} term does a slightly better job near normal angles (33°), and comes closer to the experimental intensity for the feature at $\Theta \approx 52°$.

Figures 33 and 34 show the results for the trilayer and bilayer, respectively, using the HFD pair potential plus V_s plus V_3^{a-a}. The agreement between theory and experiment is qualitatively as good for these coverages as for 25 layers.

Figure 35 shows the results of calculations for the monolayer, using the HFD pair potential plus V_s, with $V_3^{a-a} + V_3^{a-s}$ [Fig. 35(a)], and with $V_{3,C}^{a-a}$ [Fig. 35(b)]. Since V_3^{a-a} is nearly identical to $V_{3,C}^{a-a}$ for the monolayer, a comparison shows the effect of V_3^{a-s}. Within the mesh size of these calculations, the inclusion of this term has little effect on the positions of the features in the spectra. The overall shape of the calculations is similar to the experimental data. However, unlike the calculations for the multilayers, the fea-

tures show a pronounced shift towards more glancing angles relative to the experimental data. This indicates that, for the monolayer, the bound levels of the potentials are too deep.

CONCLUSIONS

In this paper, we have examined the elastic scattering of He from ordered overlayers of Ar, Kr, and Xe physisorbed on a Ag(111) substrate. This was done on a layer-by-layer basis for 1, 2,3, and ≥ 25 layers. Two types of measurements were reported in detail. In the first type, He diffraction, we measured the intensity of He scattering as a function of detector angle, while holding the incident angle constant. In the second type, selective adsorption, we monitored the peak specular intensity as a function of incident angle.

The intent of this study was to assess the relative contributions that various He–rare gas pair potentials, nonadditive multibody terms, and He–substrate interactions might make to the overall He–surface potential. It was also hoped, that by making measurements on both monolayers and thick films, that the substrate contributions to the total potential could be separated from those of the adlayers. The actual assessments were carried out by comparing the experimental data with the results of converged, close-coupled quantum scattering calculations. These comparisons were based primarily on the shapes and angular positions of various features in the selective adsorption spectra, rather than the intensities of the features. We note, however, that the good agreement in the locations of prominent features in the calculated and experimental spectra indicate that the total potentials must be close to correct in many instances, especially in light of the extreme sensitivity that these spectra have to the total He–surface potential.

The terms that were considered in the total potential included: (i) He–rare gas pair potentials derived from gas-phase measurements, (ii) an attractive term for the He–Ag interaction of the form C_3/z^3, (iii) a three-body He–adatom–adatom repulsive term consisting of a sum of ATM triple–dipole contributions for all pairs of adatoms, and, (iv) in the case of the monolayers, a small attractive contribution due to He–adatom–substrate interaction. In the total potentials considered, only the pair potential contributed to $V_G(z)$ $(G \neq 0)$.

Selective adsorption results for 25 layers of Xe along the $\langle 01\bar{1}\rangle$ azimuth can be very well reproduced using the MS pair potential plus V_3^{a-a}. The agreement between theory and experiment becomes much poorer when the He–Xe HFD(II) pair potential is used in place of the MS pair potential, while still including the ATM triple–dipole term, V_3^{a-a}. Finally, when the V_3^{a-a} term is not included, the calculations using the HFD(II) potential reproduce the experimental data about as well as those using the MS pair potential plus V_3^{a-a}.

The above comparisons tell us several important things. First, they have shown that our experiments are sensitive to different forms of the He–Xe pair potential, even when both of these potentials reasonably reproduce gas-phase data. They also show us that our experiments are sensitive to the presence of higher order terms in the He–Xe multibody po-
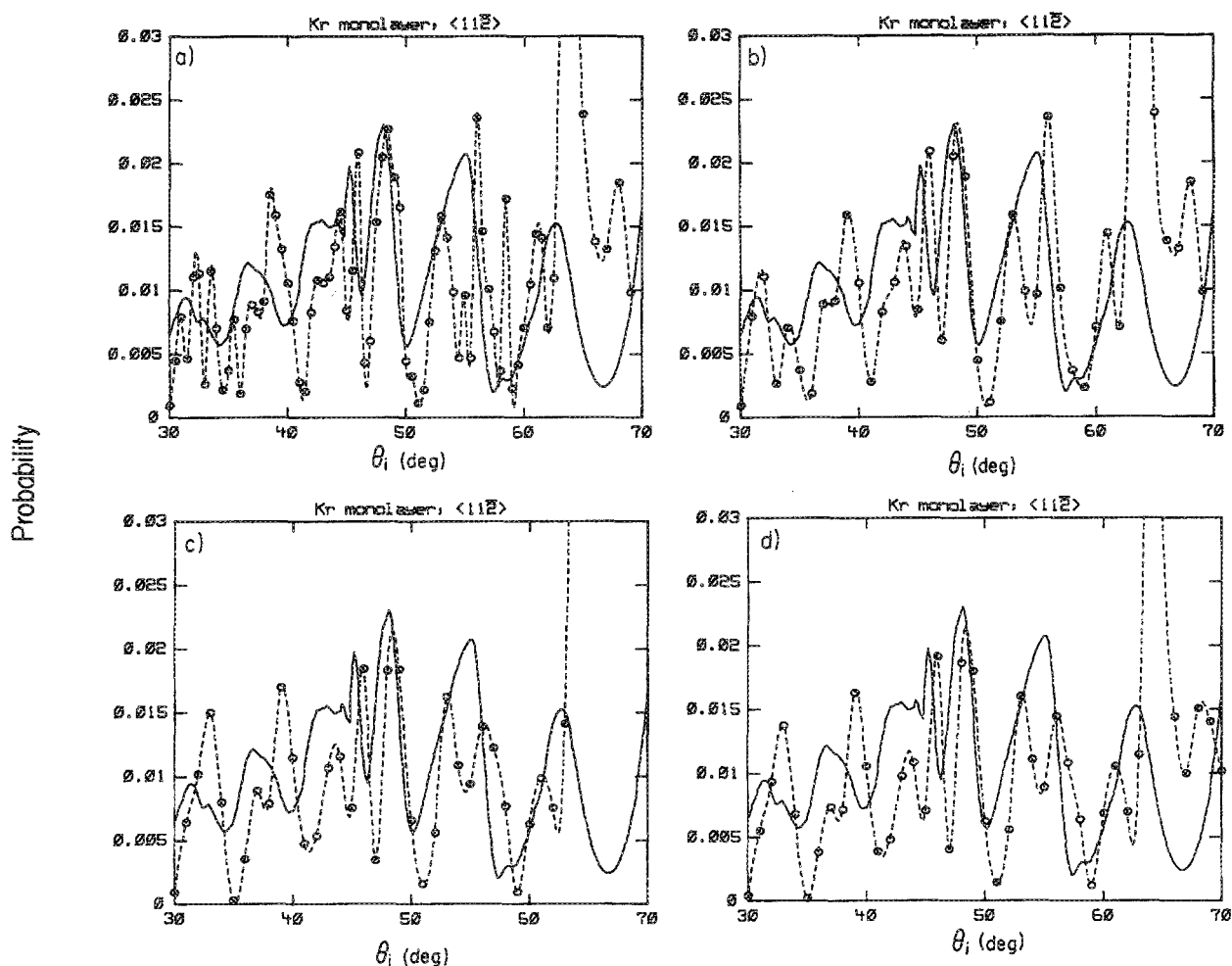
FIG. 31. Comparison between calculated and experimental results for scattering from a Kr monolayer along the $\langle 11\bar{2}\rangle$ azimuth $E = 18.051$ meV. The results plotted in (a) and (b) used the WAM pair potential plus V_s plus V_3^{a-a}. The difference between them is the angular increment of the calculations. The results shown in (c) used the WAM potential plus V_s plus V_3^{a-a} plus V_3^{a-s}. The results shown in (d) used the MS pair potential plus V_s plus V_3^{a-a} plus V_3^{a-s}.

tential expansion, i.e., shifts occur which are larger than the resolution of our experiments when V_3^{a-a} is either included or excluded from the calculations. Comparisons between selective adsorption data and scattering calculations demonstrate the *extreme* sensitivity that such measurements have to details of the He–surface potential. They also present us with a dilemma—if the two calculations, using the MS pair potential plus V_3^{a-a} and HFD(II) pair potential plus V_3^{a-a}, had agreed with each other, we would have been able to conclude that the two forms of the pair potential were nearly equivalent for our purposes, allowing us to test whether the ATM triple–dipole term is, in fact, a good representation of the overall multibody contribution to the He–Xe surface potential. Since the calculations do not agree, we cannot make this assessment. If, however, the ATM triple–dipole term is the dominant multibody contribution to the 25 layer Xe data, then our results show that the MS potential is a better representation of the He–Xe pair potential than is the HFD(II) potential, with the bound levels of the HFD(II) potential being too shallow.

Comparisons between experimental scattering results and theoretical calculations along the $\langle 11\bar{2}\rangle$ azimuth exhibit the same trends as for the $\langle 01\bar{1}\rangle$ azimuth, though the agreement between theory and experiment is somewhat poorer. The ability of the calculations to reproduce the Xe bilayer and trilayer results is similar to that for 25 layer films.

For the Xe monolayer calculations, scattering along the $\langle 01\bar{1}\rangle$ azimuth gives the best agreement. It appears that the calculations using the MS pair potential plus V_s plus V_3^{a-a} give slightly better agreement than the potential when V_3^{a-s} is also included. Either potential gives levels for V_0 that are within the error bars of the experimentally determined levels. Any effect due to the small V_3^{a-s} term should show up best for features involving the lowest-lying levels and glancing angles. The peaks in the spectrum at $\Theta \approx 59°$ and at $\Theta \approx 54°$, shown in Figs. 10(a) and 22, would be associated with E_0 and E_1 of the G_{10} and G_{11} reciprocal lattice vectors. In fact, there is a definite shift in the angular positions of these two features between the results of the calculations using the two slightly different He–surface potentials. Again, when the MS pair potential is replaced with the HFD pair potential, the agreement is much worse. Along the $\langle 11\bar{2}\rangle$ azimuth, the agreement is again not as good as was the case for Xe along the $\langle 01\bar{1}\rangle$ azimuth. In this case, the inclu-
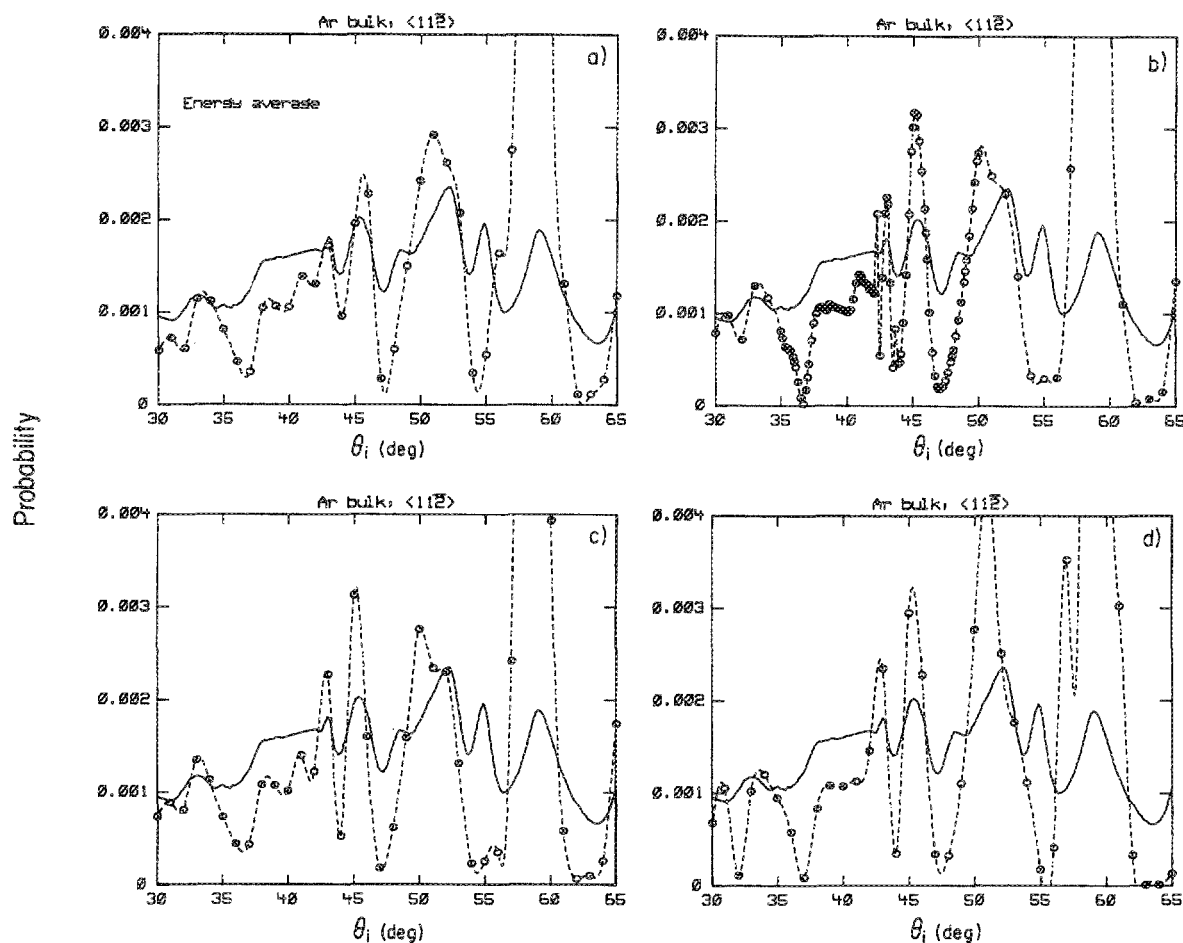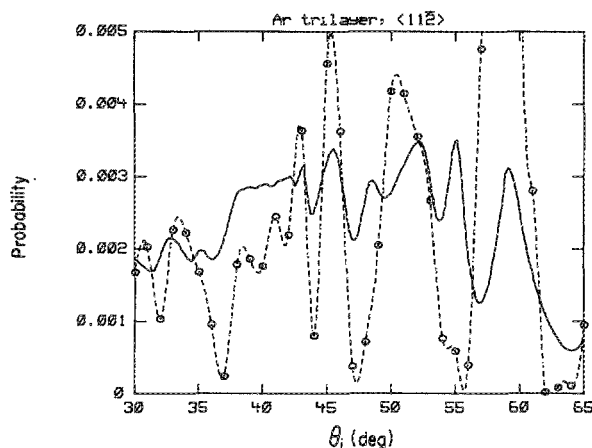
FIG. 32. Comparison between calculated and experimental results for scattering from 25 layers of Ar along the $\langle 11\bar{2}\rangle$ azimuth. The calculations shown in (a) are an average of calculations at three different energies to take into account the velocity spread of the incident beam (see the text). The total potential was composed of the HFD pair potential plus V_s plus $V_{3,C}^{a-a}$. (b) shows the results for only the central energy, 18.028 meV, which is the same energy used for the results plotted in (c) and (d). (c) shows calculations using the HFD pair potential plus V_s plus V_3^{a-a}. (d) shows calculations using the HFD pair potential plus V_s.

sion of V_3^{a-s} does not make much difference, at least over the angular range compared.

Our studies on Kr films indicated that, within our experimental resolution we could not distinguish between cal-

culated results using either the WAM or MS pair potentials. This is not surprising, as these potentials are quite similar, and produce He–surface potentials having nearly identical bound levels. The Kr monolayer calculations indicated a lack of sensitivity to the small V_3^{a-s} term. However, the

FIG. 33. Comparison between calculated and experimental results for scattering from an Ar trilayer along the $\langle 11\bar{2}\rangle$ azimuth $E = 18.032$ meV. The potential used was the HFD pair potential plus V_s plus V_3^{a-a}.
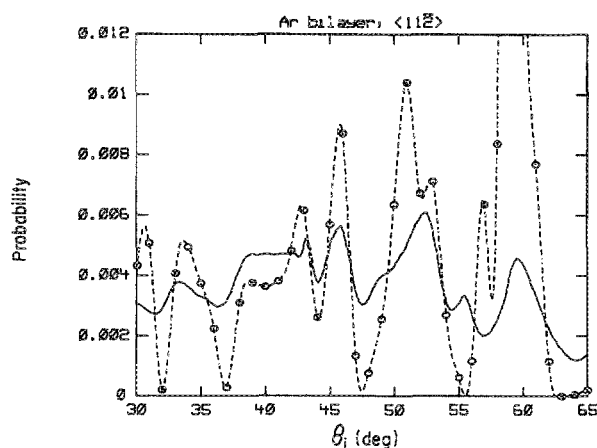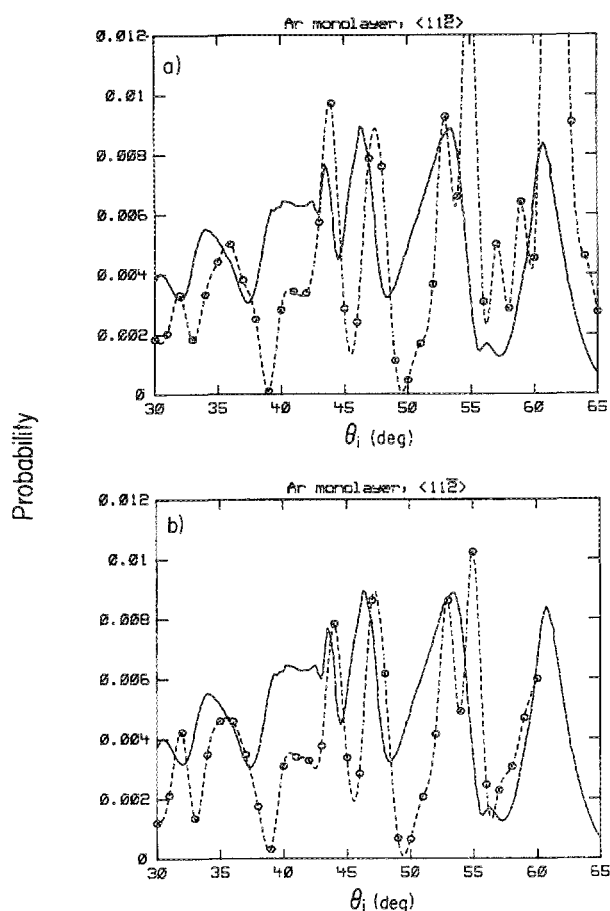

FIG. 34. Comparison between calculated and experimental results for scattering from an Ar bilayer along the $\langle 11\bar{2}\rangle$ azimuth $E = 18.032$ meV. The potential used was the HFD pair potential plus V_s plus V_3^{a-a}.

FIG. 35. Comparison between calculated and experimental results for scattering from an Ar monolayer along the $\langle 11\bar{2}\rangle$ azimuth $E = 18.015$ meV. The results plotted in (a) used the HFD pair potential plus V_s plus V_3^{q-a} plus V_3^{q-s}. The results plotted in (b) used the HFD pair potential plus V_s plus $V_{3,C}^{q-a}$.

agreement between theory and experiment was poorer than for the bilayer, trilayer, and thick film results. The features in the monolayer calculations showed a shift towards more glancing angles with respect to the experimental data. This indicates that the bound levels of the laterally averaged potential are too deep, even when the He–surface potential does not include the V_3^{q-s} term.

Finally, Ar films were also studied. In principle, the He–Ar pair potential is the most accurately known. It appears that the calculations are in better agreement with experiment for the total He–surface potential that includes V_3^{q-a}. However, the agreement is not so much better that any firm conclusions can be made about the contributions of multibody terms to the total potential. Scattering from the bilayer and trilayer show similar trends as for the bulk. Unlike the multilayers, the features in the calculations for the monolayer show a pronounced shift towards more glancing angles relative to the experimental data. This, once again, indicates that the bound levels of the calculated He–Ar monolayer/Ag potentials are too deep. We also found that the changes in the monolayer selective adsorption calculations with or without the V_3^{q-s} term are too small too resolve with an 18 meV beam.

At least for Ar and Kr, when using He–surface potentials that reasonably reproduce the multilayer data, there is a shift in the angular positions of the features in the calculations to larger angles with respect to the experimental data. As previously mentioned, this indicates that the levels of the laterally averaged potentials are too deep. This is especially true for the Ar monolayer. In this case, even the ± 0.02 Å uncertainty in the lattice constant would not effect the results enough to account for the shift. We did not do enough calculations to determine whether uncertainty in the position of the Ag reference plane z_0 alone can explain this result. Increasing b by 0.4 Å causes the lowest level of the monolayer potential to change by 0.36 meV, but only changes the lowest bound level of the bilayer potential by 0.06 meV. Thus, a fairly large change in z_0 has a much larger effect on the monolayer calculations than on the multilayer calculations.

When this study was initiated, it was hoped that elastic scattering of He from ordered rare gas surfaces would yield detailed information about the nature of the multibody expansion of the He–surface potential, i.e., which higher order terms should be included in the expansion of the potential, and about the magnitude of these terms. This premise was implicitly based upon the assumption that the He–RG pair potentials [RG = Ar, Kr, Xe] were sufficiently refined so that they observed discrepancies between the data and calculations could be attributed to the effects of higher order terms in the potential. This, unfortunately, was not necessarily the case. Our results have called into question the accuracy of the He–Xe, and possibly the He–Kr, pair potentials. Changes in these two potentials have, in fact, recently been suggested by Danielson and Keil.[60]

Since the He–Ar pair potential is believed to be accurate, the observed differences between the calculated and experimental results for He scattering from Ar(111) multilayers may be in part due to using elastic calculations. This could be especially true for regions in the spectra where the positions of features agree, but the intensities do not. With an 18 meV incident energy, these systems exhibit a significant amount of inelastic scattering. Calculations which take into account both elastic and inelastic scattering may be needed to model these systems.

ACKNOWLEDGMENTS

[1] K. D. Gibson and S. J. Sibener, Faraday Discuss. Chem. Soc. **80**, 203 (1985).
[2] K. D. Gibson and S. J. Sibener, J. Chem. Phys. **88**, 7862 (1988).

[3]K. D. Gibson and S. J. Sibener, J. Chem. Phys. **88**, 7893 (1988).

[4]K. D. Gibson and S. J. Sibener, Phys. Rev. Lett. **55**, 1514 (1985).

[5]K. D. Gibson and S. J. Sibener, J. Vac. Sci. Technol. A **3**, 1453 (1985).

[6]K. D. Gibson, S. J. Sibener, B. M. Hall, D. L. Mills, and J. E. Black, J. Chem. Phys. **83**, 4256 (1985).

[7]J. A. Barker, *Rare Gas Solids*, edited by M. L. Klein and J. A. Venables (Academic, New York, 1976), Vol. 1, Chap. 4.

[8]W. J. Meath and R. A. Aziz, Mol. Phys. **52**, 225 (1984).

[9]T. H. Ellis, G. Scoles, and U. Valbusa, Surf. Sci. **118**, L251 (1982).

[10]T. H. Ellis, S. Iannotta, G. Scoles, and U. Valbusa, Phys. Rev. B **13**, 2307 (1981).

[11]T. H. Ellis, G. Scoles, and U. Valbusa, Surf. Sci. **155**, 499 (1985).

[12]J. Z. Larese, W. Y. Leung, D. R. Frankl, N. Holter, S. Chung, and M. W. Cole, Phys. Rev. Lett. **54**, 2533 (1985).

[13]G. Bracco, P. Cantini, E. Cavanna, R. Tatarek, and A. Glachant, Surf. Sci. **136**, 169 (1984).

[14]H. Jónsson, J. H. Weare, T. H. Ellis, G. Scoles, and U. Valbusa, Phys. Rev. B **30**, 4203 (1984).

[15]J. M. Hutson and C. Schwartz, J. Chem. Phys. **79**, 5179 (1983).

[16]C. Schwartz, Phys. Rev. B **34**, 2834 (1986).

[17]H. Jónsson and J. H. Weare, Faraday Discuss. Chem. Soc. **80**, 29 (1985).

[18]C. A. Becker, Ph. D thesis, University of Chicago (1980).

[19]J. Lapujoulade, Surf. Sci. **108**, 526 (1981).

[20]K. Kern, R. David, R. L. Palmer, and G. Comsa, Phys. Rev. Lett. **56**, 2823 (1986).

[21]P. I. Cohen, J. Unguris, and M. B. Webb, Surf. Sci. **58**, 429 (1976).

[22]J. Unguris, L. W. Bruch, E. R. Moog, and M. B. Webb, Surf. Sci. **109**, 522 (1981).

[23]G. Lilienkamp and J. P. Toennies, J. Chem. Phys. **78**, 5210 (1983).

[24]J. M. Ziman, *Principles of the Theory of Solids* (Cambridge University, Cambridge, 1986), p. 56.

[25]H. Chow and E. D. Thompson, Surf. Sci. **59**, 225 (1976).

[26]K. L. Wolfe and J. H. Weare, Phys. Rev. Lett. **41**, 1663 (1978).

[27]V. Celli, N. Garcia, and J. Hutchison, Surf. Sci. **87**, 112 (1979).

[28]L. Greiner, H. Hoinkes, H. Kaarman, H. Wilsch, and N. Garcia, Surf. Sci. **94**, L195 (1980).

[29]J. S. Hutchison, Phys. Rev. B **22**, 5671 (1980).

[30]H. Chow and E. D. Thompson, Surf. Sci. **82**, 1 (1979).

[31]J. Lapujoulade, Y. Lejay, and G. Armand, Surf. Sci. **95**, 107 (1980).

[32]G. Armand, J. Lapujoulade, and Y. Lejay, Surf. Sci. **63**, 143 (1977).

[33]S. Chung, N. Holter, and M. W. Cole, Phys. Rev. B **31**, 6660 (1985); Surf. Sci. **165**, 466 (1986).

[34]J. R. Klein and M. W. Cole, Surf. Sci. **134**, 722 (1983).

[35]J. R. Klein and L. W. Bruch, and M. W. Cole. Surf. Sci. **173**, 555 (1986).

[36]W.-K. Liu, Phys. Rev. B **32**, 868 (1985).

[37]E. Zaremba and W. Kohn, Phys. Rev. B **13**, 2270 (1976).

[38]B. N. J. Persson and E. Zaremba, Phys. Rev. B **30**, 5669 (1984).

[39]R. A. Aziz, *Inert Gases*, edited by M. L. Klein, Springer Series in Chemical Physics (Springer, New York, 1984), Vol. 34, Chap. 2.

[40]K. M. Smith, A. M. Rulis, G. Scoles, R. A. Aziz, and V. Nain, J. Chem. Phys. **67**, 152 (1977).

[41]R. A. Aziz, P. W. Riley, U. Buck, G. Maneke, J. Schleusener, G. Scoles, and U. Valbusa, J. Chem. Phys. **71**, 2637 (1979).

[42]W. A. Steele, *The Interaction of Gases with Solid Surfaces* (Pergamon, Oxford, 1974), Chap. 2.

[43]G. C. Maitland and E. B. Smith, Chem. Phys. Lett. **22**, 443 (1973).

[44]K. Watanabe, A. R. Allnatt, and W. J. Meath, Chem. Phys. **68**, 423 (1982).

[45]K. T. Tang, J. M. Norbeck, and P. R. Certain, J. Chem. Phys. **64**, 3063 (1976).

[46]P. Korpiun and E. Lüscher, in *Rare Gas Solids*, edited by M. L. Klein and J. A. Venables (Academic, New York, 1977), Vol. 2, Chap. 12.

[47]E. Zaremba and W. Kohn, Phys. Rev. B **15**, 1769 (1977).

[48]J. Harris and A. Liebsch, J. Phys. C **15**, 2275 (1982).

[49]P. Nordlander and J. Harris, J. Phys. C **17**, 1141 (1984).

[50]S. Ossicini, Phys. Rev. B **33**, 873 (1986).

[51]L. W. Bruch, Surf. Sci. **125**, 194 (1983).

[52]C. G. Shaw, S. C. Fain, Jr., M. D. Chinn, and M. F. Toney, Surf. Sci. **97**, 128 (1980).

[53]B. M. Axilrod and E. Teller, J. Chem. Phys. **11**, 299 (1943).

[54]C. Schwartz, J. Chem. Phys. **83**, 437 (1985).

[55]A. D. McLachlan, Mol. Phys. **7**, 381 (1964).

[56]S. Rauber, J. R. Klein, M. W. Cole, and L. W. Bruch, Surf. Sci. **123**, 173 (1982).

[57]B. R. Johnson, in *Algorithms and Computer Codes for Atomic and Molecular Quantum Scattering Theory*, edited by Lowell Thomas (National Resource for Computation in Chemistry Proceedings No. 5, 1979), Vol. 1, p. 86; J. Chem. Phys. **67**, 4086 (1977); **69**, 4678 (1978).

[58]G. A. Parker, T. G. Schmalz, and J. C. Light, in *Algorithms and Computer Codes for Atomic and Molecular Quantum Scattering Theory*, edited by Lowell Thomas (National Resource for Computation in Chemistry Proceedings No. 5, 1979), Vol. 1, p. 172; J. Chem. Phys. **73**, 1757 (1980).

[59]J. W. Cooley, Math. Comp. **15**, 363 (1961).

[60]L. J. Danielson and M. Keil, J. Chem. Phys. (submitted).